Controls on the formation and stability of gas hydrate-related bottom-simulating reflectors (BSRs): A case study from the west Svalbard continental slope

Haake, RR; Westbrook, Graham; Riley, Michael

DOI:
10.1029/2007JB005200

JOURNAL OF GEOPHYSICAL RESEARCH, VOL. 113, B05104, doi:10.1029/2007JB005200, 2008

Controls on the formation and stability of gas hydrate-related bottom-simulating reflectors (BSRs): A case study from the west Svalbard continental slope

R. Ross Haacke,[1,2] Graham K. Westbrook,[1] and Michael S. Riley[1]

Received 1 June 2007; revised 22 December 2007; accepted 7 February 2008; published 29 May 2008.

[1] The growth and stability of the free-gas zone (FGZ) beneath gas-hydrate related bottom-simulating seismic reflectors (BSRs) is investigated using analytical and numerical analyses to understand the factors controlling the formation and depletion of free gas. For a model based on the continental slope west of Svalbard (a continental margin of north Atlantic type), we find that the FGZ is inherently unstable under a wide range of conditions because upward flow of under-saturated liquid depletes free gas faster than it is produced by hydrate recycling. In these scenarios, the 150-m-thick FGZ that presently exists there would deplete within 10^5–10^6 years. We suggest the FGZ is in a stable state, however, that is formed by a diffusion-dominated mechanism that produces low concentrations of gas in a FGZ of steady state thickness. Gas forms across a thick zone because the upward fluid flux is relatively low and because the gas–water solubility decreases to a minimum several hundred meters below the seabed. This newly understood solubility-curvature effect is complementary to hydrate recycling, but becomes the most important factor controlling the presence and properties of the BSR in environments where the rate of upward fluid flow and the rate of hydrate recycling are both relatively low (i.e., rifted continental margins). If the present-day FGZ is in steady state, we estimate that the upward fluid flux in the west Svalbard site must be less than 0.15 mm a^{-1}.

Citation: Haacke, R. R., G. K. Westbrook, and M. S. Riley (2008), Controls on the formation and stability of gas hydrate-related bottom-simulating reflectors (BSRs): A case study from the west Svalbard continental slope, *J. Geophys. Res.*, *113*, B05104, doi:10.1029/2007JB005200.

1. Introduction

[2] Marine gas hydrates are commonly associated with a bottom-simulating seismic reflector (BSR) that is evident on low-frequency seismic reflection sections [e.g., *Shipley et al.*, 1979; *Hyndman and Spence*, 1992]. This BSR lies at or near the predicted base of the gas hydrate stability zone (GHSZ), and is caused by the acoustic impedance contrast between overlying sediments containing gas hydrate and underlying sediments containing free gas [e.g., *MacKay et al.*, 1994]. Most of the reflection amplitude is caused by the low seismic velocity of the free gas zone (FGZ) beneath the BSR, which typically occupies less than a few percent of pore space in a zone up to a few hundred meters thick [e.g., *Singh et al.*, 1993; *MacKay et al.*, 1994; *Holbrook*, 2001; *Hyndman et al.*, 2001; *Bunz et al.*, 2005; *Carcione et al.*, 2005]. Observation of the BSR is important for identifying the presence of gas hydrate and underlying free gas, and consequently for quantifying the amount of natural gas hydrate existing in continental margins. However, the formation mechanisms of the FGZs that gives rise to seismically observable BSRs, and the conditions under which these FGZs can exist, are poorly understood. Here we investigate the conditions under which the FGZ (and thus the BSR) is stable, and explore the primary physical controls on its presence and properties. If the FGZ is not stable, we seek to determine the timescales in which it depletes. We use observations from an area of BSR occurrence in the continental margin of western Svalbard to constrain a numerical model for the formation and evolution of the FGZ. The area is an example of a passive, north Atlantic continental margin, but the results of the modeling are more generally applicable to all types of tectonic environment.

1.1. Introduction to the Method

[3] We conduct numerical simulations of the sub-BSR FGZ with a method that is similar to that of *Davie and Buffett* [2001]. The main difference with that work is our inclusion of a gas–water solubility curve that changes with depth (i.e., one that is calculated from the pressure and temperature). The simulations reported by *Davie and Buffett* [2001] and *Davie and Buffett* [2003a], show that the gas hydrate distribution reaches a quasi-steady state, while their use of a constant gas–water solubility beneath the GHSZ allows the underlying FGZ to grow continuously and without limits on its thickness. Our inclusion of a gas–water solubility curve that varies with depth introduces limits on FGZ growth and, when

[1]School of Geography, Earth and Environmental Sciences, University of Birmingham, Edgbaston, UK.
[2]Now at Geological Survey of Canada, Pacific Geoscience Centre, BC, Canada.

0148-0227/08/2007JB005200$09.00

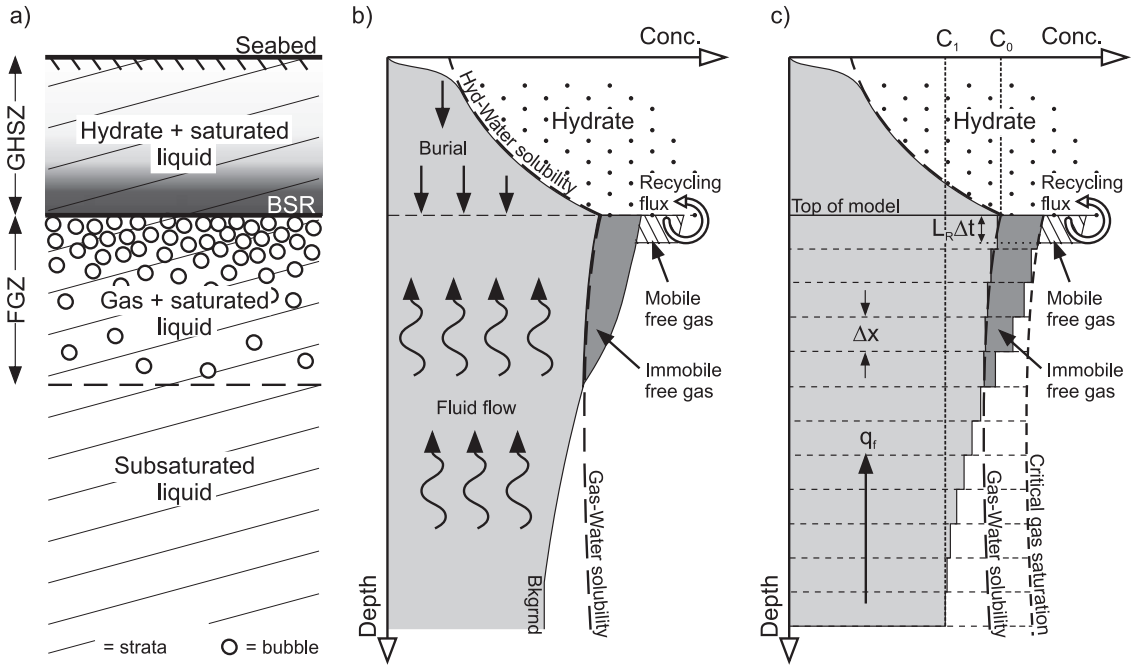

Figure 1. (a) Schematic representation of a typical marine gas-hydrate system. (b) Gas–water and hydrate–water solubility curves with the likely distribution of dissolved gas shown in light grey and immobile free gas in dark grey. Hydrate is formed from gas in solution as the solubility decreases progressively toward the seabed within the GHSZ. Ongoing sedimentation carries the hydrate toward, and through, the base of the GHSZ. Mobile free gas produced by hydrate recycling quickly migrates upward to leave immobile gas at the critical saturation. Immobile free gas occupies a thick region beneath the GHSZ. (c) Illustration of the numerical model.

the gas phase is stable, allows the FGZ to reach a quasi-steady state too. The timescale of our simulations is long enough (thousands to millions of years) that we can determine the long-term properties of the FGZ in slowly evolving systems (i.e., the low flux systems typical of tectonically passive environments). In this work we draw tighter focus on the behavior of the sub-BSR FGZ by simplifying the problem of the formation and evolution of overlying gas hydrate to one of quantifying boundary conditions at the hydrate–liquid–gas triple point (the base of the GHSZ).

1.2. Introduction to the Model

[4] The model (Figure 1) is based on the concepts described by *Hyndman and Davis* [1992], where dissolved gas is transported in upward-moving pore water to form hydrate in the GHSZ when the concentration of gas in solution exceeds solubility. The hydrate–water solubility decreases exponentially with decreasing depth below the seabed [*Zatsepina and Buffet*, 1998], enabling hydrate to form across a thick zone above the depth at which the upward-moving pore waters first become saturated. The solid hydrate is trapped in the sediment matrix and is moved downwards, toward the base of the GHSZ, by sedimentation, tectonic thickening and seabed uplift, an increase in the geothermal gradient, or a fall in sea level. If this downward flux of hydrate is rapid enough, the solid hydrate is carried through the base of the GHSZ where it dissociates to produce free gas and water. If the amount of free gas produced by dissociation is large enough, the gases become mobile and migrate upward to re-form hydrate in the GHSZ, a process known as hydrate recycling [*Kvenvolden et al.*, 1983; *Minshull and White*, 1989]. This recycling leaves a residue of free-gas bubbles trapped in the sediment matrix by capillary forces [*Schowalter*, 1979].

[5] We argue that over periods of many thousands of years, the mobile gas phase produced by hydrate dissociation can be neglected as the secular properties of the FGZ are defined mainly by the immobile gas phase that either forms in situ, or is left as a residue after the migration of mobile free gas. Many seismic observations of BSRs and their underlying FGZs indicate that the free gas is typically immobile and is not an interconnected body of buoyant gas. These observations include

[6] (1) the absence of reflections from a gas water contact at the base of the FGZ, with very few local exceptions [e.g., *White*, 1977]. In the case of our west Svalbard study area, the gradual downward decrease in the low P-wave velocity anomaly below the BSR [*Westbrook et al.*, 2005] indicates that the low levels of gas saturation in this zone cannot flow to maintain a uniform concentration;

[7] (2) the generally crosscutting nature of the BSR in relation to strata and vertical faults over distances of many tens of km, often with little or no localized variation in amplitude that would indicate a connected body of free gas is trapped beneath the BSR in a traditional caprock sense [e.g., *Hyndman et al.*, 1994];

[8] (3) low levels of gas saturation in the FGZ (typically less than a few percent of pore volume) indicated by the inversion of data from sonic logs, VSPs and seismic reflection surveys [e.g., *Helgerud et al.*, 1999; *Holbrook*, 2001; *Bunz et al.*, 2005; *Carcione et al.*, 2005];

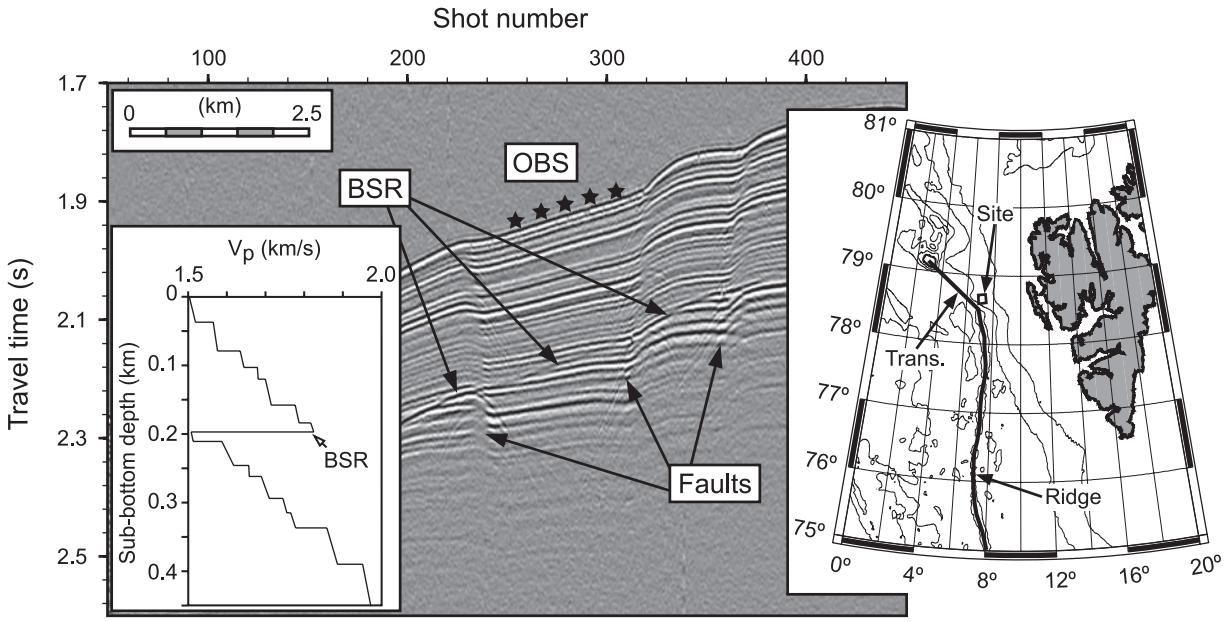

Figure 2. Map shows the location of the study area (marked by a box) at the base of the continental margin west of Svalbard and near to the junction of the Knipovich Ridge and Molloy Transform. The seismic section is from a short-offset streamer passing over the OBS used to derive *P wave* velocities (V_p) on a dip-parallel line [*Westbrook et al.*, 2005].

[9] (4) the absence of any noticeable escapes of free gas where BSRs have been penetrated by drilling during the Ocean Drilling Program or the Integrated Ocean Drilling Program.

[10] The neglect of mobile gases below the BSR is partly justified by our application to understanding the regional, as opposed to local, properties of the sub-BSR FGZ; mobile gases are the likely cause of high concentrations of hydrate in local fluid escape structures [*Liu and Flemings*, 2007], but are not a first-order component of widespread, regional, BSR formation, which is dominated by the movement of gas-rich liquids [*Hyndman and Davis*, 1992].

[11] Using a numerical algorithm, solved in one dimension with a Crank-Nicolson finite-difference routine, we quantify the response of immobile gas in the sub-BSR FGZ to a range of parameters in order to determine the strongest controls on its formation and depletion. We find that the FGZ, and consequently the BSR, is intrinsically unstable over a wide range of model space. We also find that when the FGZ is stable, the gas produced by dissociation of hydrate driven by continuous sedimentation is not, by itself, an adequate explanation for the seismically derived properties of the west Svalbard FGZ. We show that gas is produced in a quasi-steady state by a mechanism that is complementary to hydrate recycling, but which becomes dominant when the upward fluid flux is low because the gas–water solubility decreases to a minimum in the sediments below the GHSZ. Finally, by using an analytical approximation to describe the conditions under which the pore waters immediately beneath the GHSZ become saturated in terms of the upward flux of pore water, and using the observed properties of the sub-BSR FGZ as a constraint, we estimate the possible range of upward fluid flow rates at the west Svalbard study site.

1.3. Study Area

[12] The west Svalbard study area (Figure 2) lies in 1394 m of water, near the base of the continental slope and close to the junction of the Knipovich Ridge and Molloy Transform [*Vanneste et al.*, 2005a]. A prominent BSR occurs in this area at 200 ± 6 m below seafloor (mbsf), determined from traveltime inversion of ocean-bottom seismic (OBS) data [*Westbrook et al.*, 2005]. The BSR is caused almost entirely by a large reduction in P-wave velocity that extends for 150–200 m below the BSR. The low P-wave velocity is thought to be caused by the presence of free gas occupying $\leq 0.4\%$ of pore volume, if uniformly distributed [*Carcione et al.*, 2005], while the overlying gas hydrate occupies between 3 and 10% of pore volume [*Westbrook et al.*, 2008].

[13] Sediments at this west Svalbard site are low permeability, hemipelagic muds interbedded with terrigeous material deposited during the Pleistocene and early Holocene [*Eiken and Hinz*, 1993; *Vorren et al.*, 1998]. The sedimentation rate exceeds 500 m Ma^{-1} [*Eiken and Hinz*, 1993; *Vanneste et al.*, 2005a], and sediments in the region contain an appreciable amount of organic carbon. The bottom water temperature is −0.9°C [*Vanneste et al.*, 2005b]. The nearest Ocean Drilling Program (ODP) site, 986, is located in a similar geological setting 200 km to the south [*Jansen and Raymo*, 1996], and is used as a guide to the west Svalbard sediment sequence. Headspace gases obtained from site 986 are composed almost entirely of methane and we assume this to be true at the west Svalbard study site also.

2. Conceptual Model

[14] We couple observations made at the west Svalbard study area with the assumptions listed below to quantify the concentrations of methane in liquid and gas phases at the hydrate–liquid–gas triple point (the base of the GHSZ).

Using these boundary conditions as constraints on the model, we avoid the problem of the formation of overlying gas hydrate, and concentrate on the formation and evolution of the underlying gas phase. The model thus considers a continuum of sediment, seawater, and gas in a reference frame fixed to the triple point (Figure 1), which, in turn, is allowed to move relative to the sediments in response to burial, and to changes in pressure (p) and temperature (T).

2.1. Model Assumptions

[15] The model assumes:

[16] (1) hydrate is relatively abundant in pore space immediately above the base of the GHSZ, but not abundant enough to greatly reduce the sediment permeability (*Westbrook et al.* [2008] show that it is in the range 3–10% of pore volume);

[17] (2) the kinetics of phase transition can be neglected (phase change is shown to be quick by *Rehder et al.* [2002] and *Zatsepina and Buffet* [2001], among others);

[18] (3) from the assumption of rapid phase change, we further assume that the system is in thermal and chemical equilibrium;

[19] (4) the influence of capillarity on the phase equilibria of hydrate, gas and water can be neglected;

[20] (5) the mass of methane and water are conserved in the fluid phases (i.e., that chemical reactions with the sediments to not occur);

[21] (6) constant salinity of 3.5 wt % NaCl (close to average seawater);

[22] (7) constant water and sediment-grain density;

[23] (8) steady and continuous sedimentation.

[24] Prior work using some or all of these assumptions includes that of *Rempel and Buffett* [1997], *Xu and Ruppel* [1999], and *Davie and Buffett* [2001].

2.2. The Role of Hydrate Recycling and Mobile Versus Immobile Gases

[25] Gas hydrate formed by in situ methanogenesis [e.g., *Paull et al.*, 1994], or by upward flow of methane-rich solution [e.g., *Hyndman and Davis*, 1992], is concentrated near the base of the GHSZ by the process of hydrate recycling [e.g., *Kvenvolden et al.*, 1983; *Minshull and White*, 1989]. Pore water in the vicinity of the triple point is already saturated, so the gas released during hydrate recycling moves into the free gas phase. If the concentration of this free gas becomes large enough to exceed the critical gas saturation, then the excess gas overcomes capillary forces to migrate upward and exit the FGZ quickly. Mobile gas moves at speeds of mm s^{-1} in fine grained sediments to cm s^{-1} in coarser-grained media if gas moves as clusters of bubbles, or at greater speeds if the gas moves by channel flow [e.g., *Roosevelt and Corapcioglu*, 1998; *Corapcioglu et al.*, 2004; *Oldenburg and Lewicki*, 2006; *Stöhr and Khalili*, 2006].

[26] The passage of mobile gases leaves a residue of immobile free gas trapped in the pore space at the critical gas saturation [*Schowalter*, 1979]. Thus if hydrate just above the base of the GHSZ is abundant, then it is the level of critical gas saturation that determines the maximum concentration of gas being produced at the triple point by hydrate recycling (everything above that maximum migrates out of the FGZ). If gas hydrate is not abundant enough, then the concentration of gas produced during dissociation is subcritical and the mobile phase is never formed. Beneath the GHSZ, the long-term effect of hydrate dissociation during recycling is to produce an immobile free gas phase that has concentration less than or equal to the critical gas saturation. Our model does not introduce mobile gases at the bottom boundary, so we formulate the material balance without consideration of the mobile gas phase. Immobile gas in the FGZ is assumed to be distributed in a homogeneous gas/water mixture. It is introduced at the triple point at the base of the GHSZ, then transported through the model at the sediment burial velocity. This approach (including the neglect of the mobile gas phase) is taken by *Davie and Buffett* [2001] and *Davie and Buffett* [2003a], and our model formulation is similar to theirs.

2.3. Constraints on Mass Balance at the Triple Point

[27] Gas hydrate residing in the GHSZ buffers the local concentration of dissolved gas to maintain saturation at solubility levels, since this is the hydrate–liquid equilibrium state (Figure 1). Methane solubility curves in the hydrate–liquid and gas–liquid systems must intersect at the hydrate–liquid–gas triple point to ensure the solubility is continuous [*Milton*, 1976; *Zatsepina and Buffett*, 1998]. The presence of gas hydrate at, or just above, the triple point thus maintains the local concentration of dissolved gas at a value that depends on its solubility and not on the presence of free gas in the sediments below.

[28] Our model uses the gas hydrate buffer, the critical gas saturation, and the seismically derived concentration of overlying gas hydrate to formulate boundary conditions for aqueous methane concentration and free gas saturation at the triple point. The use of these boundary conditions on the aqueous and gaseous phases allows us to model everything in and below the FGZ without considering hydrate formation and dissolution within the GHSZ.

2.4. Evolution of the Free-Gas Zone

[29] In the model, the mass of free gas at each point in the FGZ is tracked in bins that are fixed to the sediment grain matrix (Figure 1c). These bins freely exchange methane between the gaseous and aqueous phases, as required by the difference between local concentrations of dissolved gas and solubility. Below the FGZ, where the concentration of dissolved methane is less than solubility, the sediment contains no hydrate or free gas and the concentration smoothly reduces to a constant background level.

[30] Fluid advection, mechanical dispersion, and chemical diffusion transport dissolved gas through the liquid phase. This aqueous transport perturbs the system and causes gas to be exchanged between the liquid and free-gas phases. As advection and dispersion evolve the model from its initial state, we allow the p–T conditions in the sediments to change in response to bottom water warming, sea level rise and fall, tectonic uplift, or sedimentation and compaction. In all these cases, the top boundary of the model is moving spatially, and the boundary conditions are time dependent (quantified with the methods described in section 3.3). In situ biogenic methanogenesis was investigated using the analytical approach of *Davie and Buffett* [2001], but was found to have a negligible impact on the results because the rates of methanogenesis are very low at

the depths of the FGZ. Consequently, this aspect of the system is not discussed further.

3. Fluid Flow and Mass Transport: Numerical Representation

[31] In a moving liquid, dissolved methane is transported by advection at the mean velocity of its solvent. The solute is also subject to dispersion, which is the mixing of fluids with different chemical composition by: (1) mechanical dispersion due to flow through a tortuous medium; (2) mechanical dispersion due to velocity variations across pore throats; (3) molecular diffusion.

3.1. Advection and Dispersion in Porous Media

[32] The model is restricted to one dimension (the vertical) following the justification by *Davie and Buffett* [2003a] and with the additional caveat that we are interested in the widespread, regionally representative FGZ rather than local accumulations of gas. In one dimension (z), transport of dissolved methane is described by the advection–dispersion equation,

$$\frac{\partial\left(\phi\left[1-S_g\right]C\right)}{\partial t}=\frac{\partial}{\partial z}\left(\phi\left[1-S_g\right]D\frac{\partial C}{\partial z}-\phi\left[1-S_g\right]u_f C\right)+Q \tag{1}$$

[*Bear*, 1979] for time t, an aqueous methane concentration C (mass per unit volume), fluid advection velocity u_f, dispersion coefficient D, porosity ϕ, gas saturation (volume fraction of pore space) S_g, and rate of mass transfer from the gaseous phase Q. The mass transfer, Q, is applied at the end of each time step and is calculated from the local solubility C_{eq} (determined from p and T) according to

$$Q=\phi\left[1-S_g\right]\left(C_{eq}-C\right)R_Q. \tag{2}$$

where R_Q is a constant controlling the rate at which the saturation anomaly ($C_{eq}-C$) is restored to equilibrium: from assumption 2, R_Q is increased to the point where equilibrium is restored within the time step of the model.

[33] The concentration of immobile free gas held at each point in the FGZ is described by

$$\frac{\partial\left(\phi S_g\rho_g\right)}{\partial t}=-\frac{\partial\left(u_s\phi S_g\rho_g\right)}{\partial z}-Q \tag{3}$$

where ρ_g is the gas density and u_s is the sediment burial velocity, given in terms of sedimentation rate $\dot{S}$ by

$$u_s(z)=\left(\frac{1-\phi_0}{1-\phi(z)}\right)\dot{S} \tag{4}$$

[*Davie and Buffett*, 2001]

[34] The porosity is assumed to be in steady state and of the form

$$\phi(z)=\phi_0 e^{-z/\lambda} \tag{5}$$

[*Athy*, 1930], where λ is the compaction length, and ϕ_0 is the seabed porosity. Equation (1) assumes that all pore volume is available to the fluid and, hence, that the liquid volume flux q_f is related to the advection velocity by

$$q_f=\phi\left[1-S_g\right]u_f. \tag{6}$$

[35] The dispersion coefficient is calculated from the free-water diffusion coefficient d_0, the tortuosity factor χ, the dispersivity α, and u_f by

$$D=\alpha|u_f|+\chi d_0. \tag{7}$$

[36] The dispersion coefficient varies spatially through its dependence on u_f, which is inversely proportional to $\phi[1-S_g]$ since q_f must be conserved for steady flow of a constant density liquid.

[37] Within each time step Δt, the recycling rate L_R is used to calculate the movement of the top model boundary relative to the sediment grains. This allows the aqueous and gaseous concentrations to be prescribed in the length of the newly created model section, $L_R\Delta t$, according to the boundary conditions. The boundary condition on aqueous methane concentration is fixed by the solubility at the triple point, C_0, while the boundary condition for the gaseous concentration is conditional: either the critical gas saturation, S_{gc}, or the concentration of gas produced by dissociation of the overlying hydrate (calculated using the approach outlined by *Xu and Germanovich* [2006]), with saturation S_h, whichever is smaller. The bottom model boundary has fixed aqueous concentration equal to the background value, C_1, and is imposed at a depth sufficiently large that it does not interfere with the active part of the system. In all our simulations we impose the condition $C_1 < C_0$, such that mobile gases are not produced by upward advection of gas-rich liquid.

[38] From an initial C, C_{eq} (calculated from p and T), L_R, and with known or prescribed system parameters q_f, C_1, d_0, χ, α, ϕ_0 and λ, the transport of methane through the system can be calculated by solving equations (1), (2) and (3). This was achieved with a finite difference algorithm using Gaussian elimination applied to the Crank-Nicholson form of equation (1), with equations (2) and (3) applied as corrections at the end of each time step. This approach is unconditionally stable when $q_f = 0$ and gives a stable and convergent solution in the case of $q_f \neq 0$ when the Peclet number ($Pe = u_f\Delta z/D$, for mesh spacing Δz) does not exceed 0.1 and the Courant number ($Co = u_f\Delta t/\Delta z$, for time step Δt) is less than 1.0 [*Huyakorn and Pinder*, 1983].

3.2. Initial Conditions and Model Configuration

[39] We start the model with an initial FGZ similar to that observed at the west Svalbard study area. The initial concentration of immobile free gas held in pore space of the FGZ is calculated in terms of a gaseous volume distribution across the FGZ, which is derived from seismic observations at the study site. Initial aqueous methane concentration in the FGZ is defined by the gas–water solubility curve.

[40] Both the gas–water solubility and the density of immobile free gas depend on the p–T conditions in the

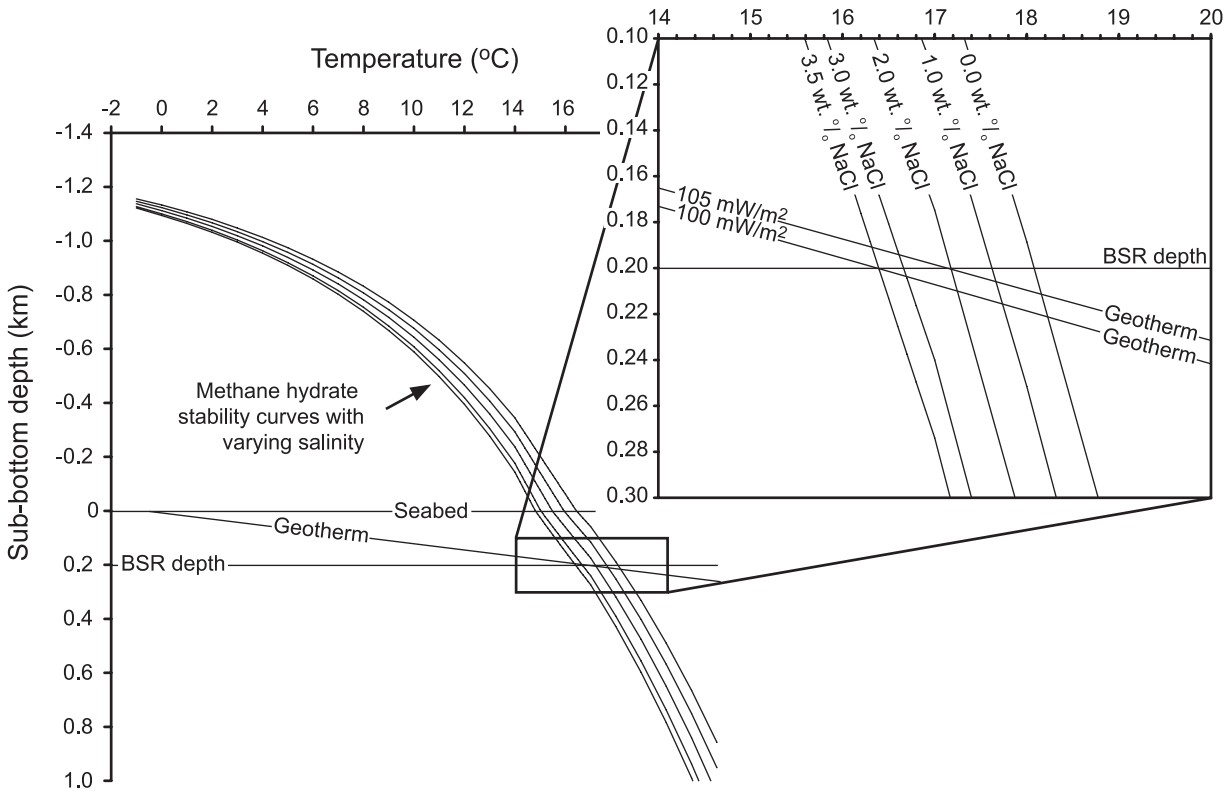

Figure 3. Methane hydrate phase stability curves for a range of salinities (0–3.5 wt.% NaCl). Pressure gradient is the mean of lithostatic and hydrostatic. Inset shows detail of these curves and their relationship to geotherms calculated for an average conductivity of 1.156 W m^{-1} K^{-1} and with heat flows of 100 and 105 mW m^{-2}.

system. However, the shape of the aqueous concentration profile in the underlying sub-saturated zone does not depend directly on p or T. This profile smoothly decreases with increasing depth to the background level and depends on the competing effects of downward diffusion from the FGZ and upward advection of liquid from the lower boundary. Initial conditions for this subsaturated zone are determined by allowing the model to relax from an initial state in which the aqueous concentration discontinuously reduces to the background at the base of the FGZ. Applying this relaxation step prior to the main calculation allows the initial conditions to approach some level of maturity and avoids any response caused by unrealistic changes of aqueous methane concentration during the main calculation.

3.2.1. Pressure and Temperature

[41] Pore fluid in the rapidly deposited, low permeability hemipelagic muds at west Svalbard is expected to be at a pressure greater than hydrostatic. We assume a mean of lithostatic and hydrostatic pressures. For the porosity of equation (5) this is written

$$p(z) = \frac{1}{2}\left(\lambda g \phi_0 \left(\rho_f - \rho_s\right)\left[1 - e^{-z/\lambda}\right] + g\rho_s z + g\rho_f z_w + g\rho_f (z + z_w)\right), \quad (8)$$

where ρ_s is the sediment grain density (2700 kg m^{-3}), ρ_f is the pore water density (1030 kg m^{-3}), g is the acceleration due to gravity (9.81 m s^{-2}), z_w is the overlying water depth (1394 m) and z is the depth below seafloor. The porosity is found by fitting equation (5) to measured porosities from ODP sites 986 C and D.

[42] The near-surface geotherm is estimated using the observed BSR depth (200 ± 6 mbsf) to find the temperature at the base of the GHSZ. This temperature is evaluated from the phase equilibria conditions of pure methane hydrate in water with 3.5 wt. % NaCl [*Sloan*, 1990]. Using an average thermal conductivity of 1.156 W m^{-1} K^{-1} [*Jansen and Raymo*, 1996] and a bottom water temperature of −0.9°C, we find that a heat flow of 100 mW m^{-2} (i.e., a near-surface geothermal gradient of 86.5 °C km^{-1}) is required for the steady state geotherm to intersect the methane hydrate stability curve at 200 mbsf (Figure 3). The geotherm is an underestimate if the salinity is less than 3.5 wt %, or if the pressure is closer to lithostatic. The difference for geotherms caused by a change in salinity of ±1 wt. % NaCl is within the likely error of estimation from these methods [*Grevemeyer and Villinger*, 2001].

3.2.2. Free-Gas Concentration

[43] The density of methane in the immobile gaseous phase (ρ_g) is calculated from the ideal gas equation,

$$\rho_g = \frac{p}{RT} \mathrm{M}_{\mathrm{CH_4}} \quad (9)$$

where $\mathrm{M_{CH4}}$ is the relative molecular mass of methane and R is the universal gas constant. More accurate equations-of-

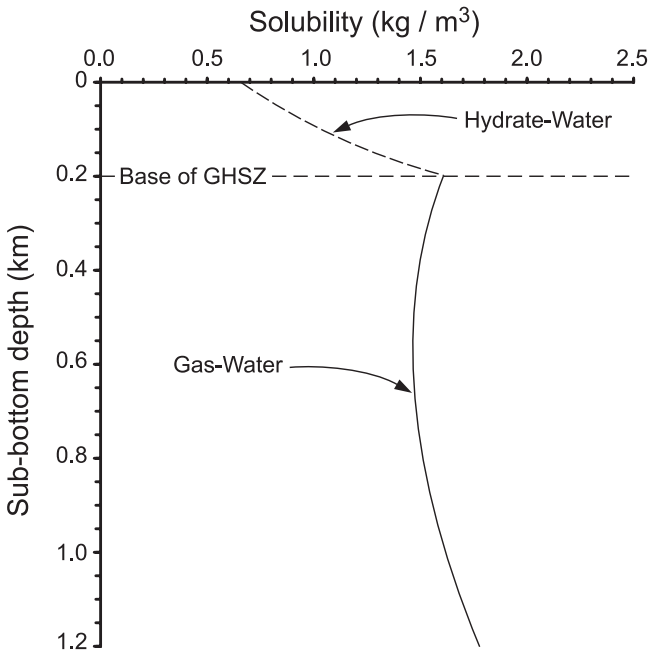

Figure 4. Methane gas–water solubility (solid line) calculated by the method of *Duan et al.* [1992a] with a linear geothermal gradient of 86.5°C km^{-1}, a mean of lithostatic and hydrostatic pressure gradients and salinity of 3.5 wt.% NaCl. The hydrate–water solubility (dashed line) is drawn schematically.

state make little difference to the gas density under the pressures and temperatures of interest to this study.

3.2.3. Methane Solubility

[44] Gas–water solubility is calculated from the method of *Duan et al.* [1992a], with the equation of state for methane that of *Duan et al.* [1992b]. The solubility curve, shown in Figure 4 for Svalbard, quantifies the boundary condition of dissolved-gas concentration at the base of the GHSZ and also quantifies the concentration in all parts of the system coexisting with free gas.

3.3. Dynamic Boundary Conditions: Mechanisms for Hydrate Recycling

[45] The upper boundary of the model is fixed to the hydrate–liquid–gas triple point and is thus subject to dynamic boundary conditions driven by the mechanisms causing hydrate recycling. In this section we summarize the methods and results of a quantitative approach to representing the motion of the triple point in response to hydrate recycling in the west Svalbard system.

3.3.1. Hydrate Dissociation Due to Sedimentation

[46] Continuous sedimentation causes individual sediment grains to move downward relative to the base of the GHSZ, the depth of which is tied to the seabed by the local geotherm. Gas hydrate trapped in the sediment pore space dissociates as it moves from the GHSZ and into a warmer part of the subsurface. Sedimentation also reduces the pressure at a constant depth below seafloor by decreasing water depth (z_w) as the sediment column lengthens, although this is partially offset by isostatic compensation as additional mass added to the seafloor causes subsidence of the oceanic crust.

[47] By conserving solid sediment volume and assuming a steady state compaction curve (Appendix A), we find the rate of seabed movement is given by

$$\frac{dz_w}{dt} = \dot{S}[1-\phi_0]\left(\frac{\rho_s}{\rho_m} - \frac{1}{[1-\phi_m]}\right), \tag{10}$$

where $\dot{S}$ is the sedimentation rate, ϕ_m is the porosity at maximum compaction and ρ_m is the mantle density (3300 kg m^{-3}). With $\phi_m = 0.06$, a median value for shales [*Allen and Allen*, 2005], and the porosity defined by equation (5) and the values in Table 1, the seabed movement is $dz_w/dt = -0.11\ \dot{S}$, where the negative sign indicates upwards motion. We note that the west Svalbard site is likely to be undergoing thermal subsidence, but ignore this effect as it is expected to be small. We also note that the geothermal gradient will be decreased by rapid sedimentation, but the effect of this on the base of the GHSZ is small in comparison with the relative vertical motion of the sediment.

[48] The hydrate recycling caused by continuous sedimentation is described in two stages. The first is the burial of sediments past a fixed point below the seabed, given by dz_w/dt. The second is the shift of the hydrate phase equilibria curve, relative to the seabed, due to upward seafloor movement and the consequent reduction in pressure (we assume constant bottom water temperature). The rate of movement of the triple point relative to the sediment grains (L_R) is thus

$$L_R = \frac{dz_w}{dt} + \frac{dz_{gh}}{dz_w}\frac{dz_w}{dt}, \tag{11}$$

where dz_{gh}/dz_w can be evaluated from the trendline in Figure 5. Sediment thickening due to convergent margin accretion, and the consequent seabed uplift, can be included by an additional term in equation (10).

3.3.2. Hydrate Dissociation Due to Deglaciation

[49] The effect of climatically driven $p-T$ perturbations on the GHSZ have been modeled by, among others, *Foucher et al.* [2002] at the Nankai slope, *Jung and Vogt* [2004] on the Norwegian margin, *Bangs et al.* [2005] at Hydrate Ridge, and *Mienert et al.* [2005] at the Storegga slide. Here we use the sea level data of *Fairbanks* [1989] and an estimated bottom water temperature change of +0.4°C at the end of the Y. Dryas [*Kristensen et al.*, 2003; *Mienert et al.*, 2005] to quantify the effect of Pleistocene-Holocene deglaciation on the GHSZ west of Svalbard (Appendix B).

[50] We find that the west Svalbard system is currently in a state of thermal relaxation and that the base of the GHSZ has 2 m of upward movement remaining before thermal equilibrium is reached (Figure 6). Contrary to the other examples cited, which are at lower latitudes, we find that the system is dominated by the change in sea level rather than the change in water temperature, and that the net effect of deglaciation will be to move the base of the GHSZ downwards by approximately 3 m when the system has come to thermal equilibrium.

[51] The base of the GHSZ is currently 5 m below its steady state position at the last glacial maximum. It is clear that the most recent deglaciation can not be responsible for any of the FGZ observed at the west Svalbard site unless the

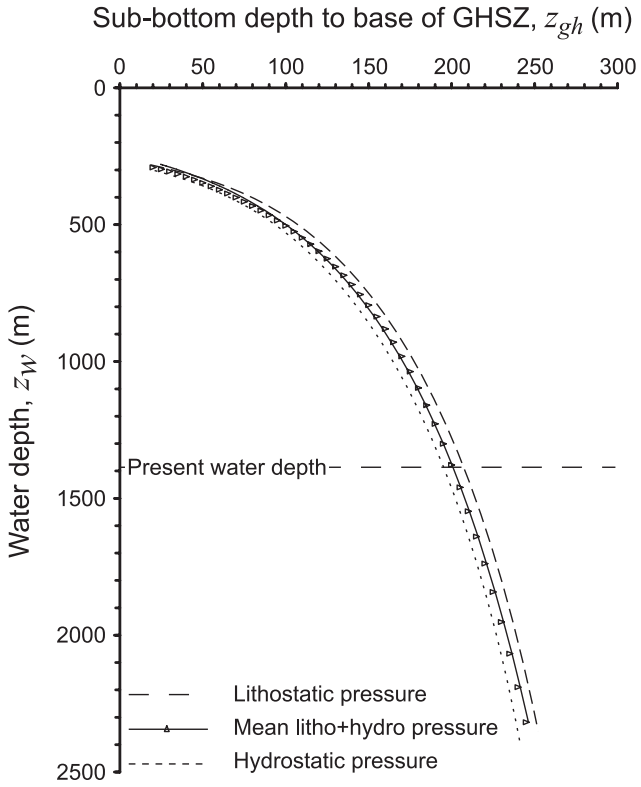

Figure 5. Sub-bottom depth to the base of the GHSZ, z_{gh}, as a function of overlying water depth, z_w. Assumes a constant bottom water temperature of -0.9°C and geothermal gradient of 86.5°C km^{-1}. The mean-pressure curve (solid line) is described by $z_{gh} = (c \ln[\frac{z_w - a}{b}])^d$, where $[a, b, c, d] = [1.3849 \times 10^2, 1.0312 \times 10^2, 7.4950 \times 10^1, 1.0137]$.

change in bottom water temperature has been significantly underestimated.

4. Model Parameterization for the West Svalbard Study Area

[52] Model parameters for the west Svalbard site are summarized in Table 1. Those parameters that have not been measured in the west Svalbard area are adopted from ODP site 986 (for the porosity and sediment properties in particular). Reference should be made to the literature noted in Table 1 for more information about these values.

4.1. Critical Gas Saturation: S_{gc}

[53] Although much work has been done on the nucleation, growth and transport of free gas in porous media [e.g., *Du and Yortsos*, 1999; *Meakin et al.*, 2000; *Marulanda et al.*, 2000; *Tsimpanogiannis and Yortsos*, 2002, 2004; *Amili and Yortos*, 2006, and references therein], it is still difficult to predict the critical gas saturation without detailed experimental knowledge of the porous medium. Nearly all critical gas saturations available in the literature are greater than a few percent of pore space [e.g., *Moulu*, 1989; *Kortekaas and Pelgeest*, 1991; *McDougall and Sorbie*, 1999], although some are as low as 0.5–1% [*Firoozabadi et al.*, 1992].

[54] *Bondino et al.* [2005] discuss the influence of the rate of formation of the gaseous phase as a control on the critical gas saturation, and show that low rates of bubble growth (rate-limited by the relatively slow diffusive transport of dissolved gas to the nucleation centre, for example) correspond to the formation of a small number of large bubbles that, as a consequence, have a low critical gas saturation when this is considered as a bulk, average, property. Most critical gas saturations in the literature are derived from observations or modeling of solution-gas drive experiments that occur on timescales of hours to days, and would produce a large number of small gas bubbles with a relatively high critical gas saturation. Gas formation in the west Svalbard gas hydrate system is likely to be slower than in a solution-gas drive experiment and so it is reasonable to expect a lower critical gas saturation.

[55] At our study site, the seismically derived hydrate concentration is in the range 3–10% of pore volume at the base of the GHSZ [*Westbrook et al.*, 2005, 2008]. At the temperatures and pressures of the BSR, the density of methane in hydrate and gaseous phases is about the same, so hydrate that dissociates during recycling should produce free gas in approximately 3–10% of pore volume. The seismically derived gas concentration immediately beneath the BSR is approximately 0.4%, however, too low to represent all the gas released during recycling. Consequently, we use 0.4% as the initial value of critical gas saturation, but explore the consequences of higher values while testing the sensitivity of the model. (Note that the model varies almost linearly for values of critical gas saturation in the range 0.1–1%, so it is straightforward to predict the effect of small changes to this parameter.)

4.2. Fluid Flux: q_f

[56] Another parameter of particular importance is the upward flux of liquid that is prescribed at the bottom boundary of the model. Studies of fluid expulsion in accretionary prisms indicate that the volume flux expected from tectonically driven compaction is typically about -1.0 mm a^{-1} [*Wang et al.*, 1993; *Hyndman et al.*, 1993]. The value in margins with no tectonic consolidation is likely to be much less: in the simple case of one-dimensional gravitational compaction of clastic sediments, the net movement of fluid is downward relative to the seabed [*Hutchison*, 1985]. *Davie and Buffett* [2003b] show that with a net downward movement of fluid, gas hydrate is unlikely to accumulate to observable concentrations as biogenic methanogenesis does not produce methane rapidly enough to compete against upward methane diffusion that depletes hydrate in the GHSZ [see also *Zatsepina and Buffett*, 1998]. The presence of a BSR at the west Svalbard site thus indicates that the net fluid flux is toward the seabed. *Egeberg and Dickens* [1999] find fluid advection rates of -0.2 mm a^{-1} for the Blake Ridge contourite drift, a magnitude generally supported by the numerical analyses of *Davie and Buffett* [2001, 2003a, 2003b] and *Buffet and Archer* [2004]; we expect a similar magnitude at the west Svalbard site and prescribe an initial value of -0.1 mm a^{-1}.

4.3. Background Methane Concentration: Bottom Boundary Condition, C_1

[57] The background methane concentration in this study, C_1, is that which enters the model through the deeper boundary. It is likely that the background is some significant

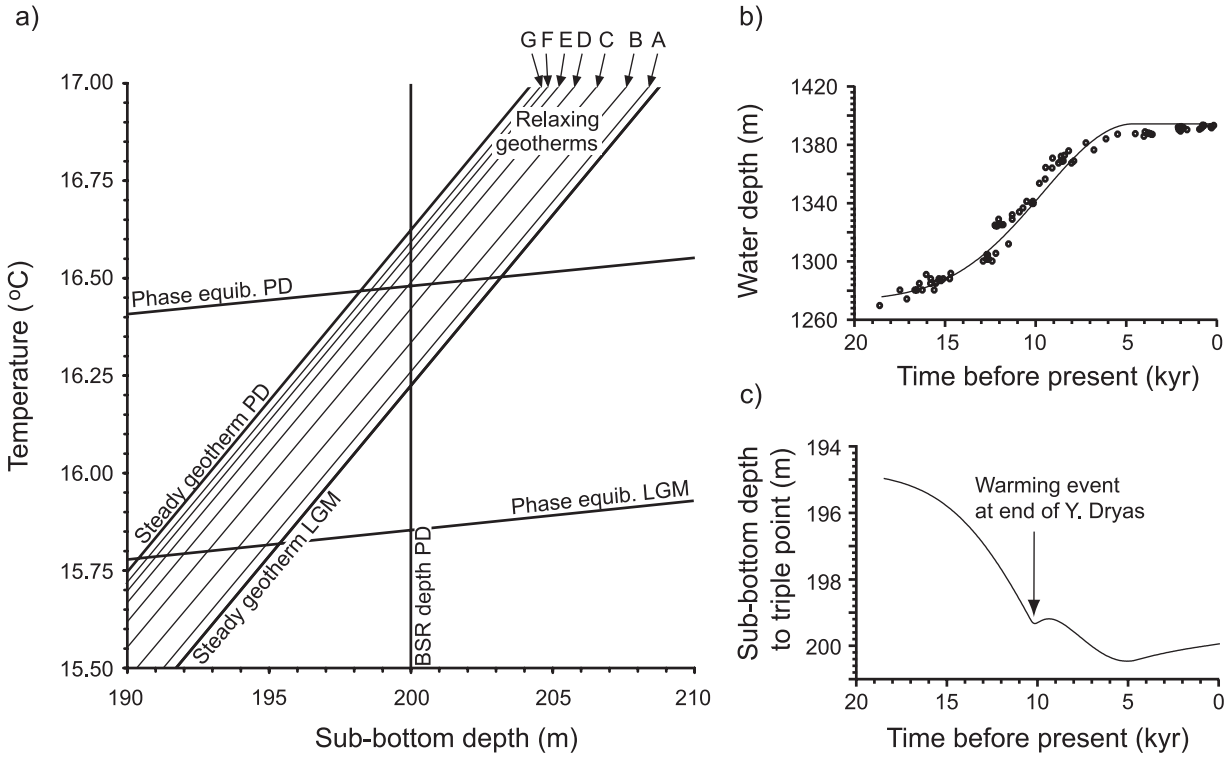

Figure 6. Effect of Pleistocene-Holocene deglaciation on sub-bottom depth to the triple point at the west Svalbard site: (a) Steady state geotherms and methane hydrate phase equilibria conditions for the present-day (PD) and last glacial maximum (LGM). The curves are calculated with a heat flow of 100 mW m^{-2}, see Appendix B for details. Also shown are the relaxing geotherms calculated for a range of times since sudden bottom water warming by +0.4°C. Time contours (yrs) are given for the following powers of ten: A,B,C,D,E,F,G = 2.8,3.2,3.6,4.0,4.4,4.8,5.2. (b) Sea level data from *Fairbanks* [1989], with a Gaussian trendline superimposed (Appendix B). (c) Temporal dependence of triple point depth given the sea level curve in (b) and a bottom water warming event of +0.4°C at the end of the Younger Dryas.

fraction of methane solubility at the base of the GHSZ. We note, however, that the seismic data show no evidence of an accumulation of free gas near the solubility minimum, which occurs at approximately 600 mbsf at this site (Figure 4). We suggest that the background concentration is less than the solubility minimum and adopt a value of 0.8 kg m^{-3}, a value that is approximately half the concentration at the triple point.

4.4. Dispersion Parameters: D, d_0, χ and α

[58] The dispersion coefficient (D) depends not only on the free-water diffusion coefficient (d_0) but also on the advection velocity (u_f), the tortuosity factor (χ) and the dispersivity (α). The free-water diffusion coefficient depends most strongly on temperature [*Sachs*, 1998; *Lu et al.*, 2006], and at the temperatures of interest to this study (in the range 0–40°C) is approximately $2 \times 10^{-9} \pm 1 \times 10^{-9}$ m^2 s^{-1} [*Lu et al.*, 2006].

[59] The tortuosity factor is harder to quantify over the scales of methane transport in the model. We use $\chi = 0.75$, a value that is greater (less tortuous) than values obtained from measurements made in relatively low-porosity reservoir rocks [e.g., *Krooss and Leythaeuser*, 1988; *Attia*, 2005]. This is justifiable because the sediments in the top few hundred meters below the seafloor have higher porosity and are less tortuous (with χ closer to unity) than reservoir rocks.

[60] The dispersivity has dimensions of length, is scale dependent and is subject to some considerable uncertainty.

Table 1. Model Reference Parameters: [1][*Carcione et al.*, 2005]; [2][*Westbrook et al.*, 2005, 2008]; [3][*Lu et al.*, 2006]; [4][*Beicher.*, 2000]; [5][*Vanneste et al.*, 2005b]; [6][*Jansen and Raymo*, 1996]; [7][*Butt et al.*, 2000]; [8]This Paper

	Parameter	Value	Ref
C_1	background methane concentration, kg m^{-3}	0.8	8
d_0	free-water diffusion coefficient, m^2 s^{-1}	2×10^{-9}	3
q_f	fluid flux, mm a^{-1}	−0.1	8
S	sedimentation rate, m Ma^{-1}	500	2
S_h	hydrate saturation at base of GHSZ	0.03	2
	free-gas zone thickness, m	150	2
S_{gc}	critical gas saturation	0.004	1
T_0	bottom water temperature, °C	−0.9	5
	geothermal gradient, °C km^{-1}	86.5	8
	salinity (wt. % NaCl)	3.5	8
z_{gh}	depth to BSR, mbsf	200	2
z_w	water depth, m	1394	5
α	dispersivity, m	50	8
λ	porosity decay, m	1053	6
ρ_f	water density, kg m^{-3}	1030	4
ϕ_0	seafloor porosity fraction	0.555	6
χ	tortuosity factor	0.75	8

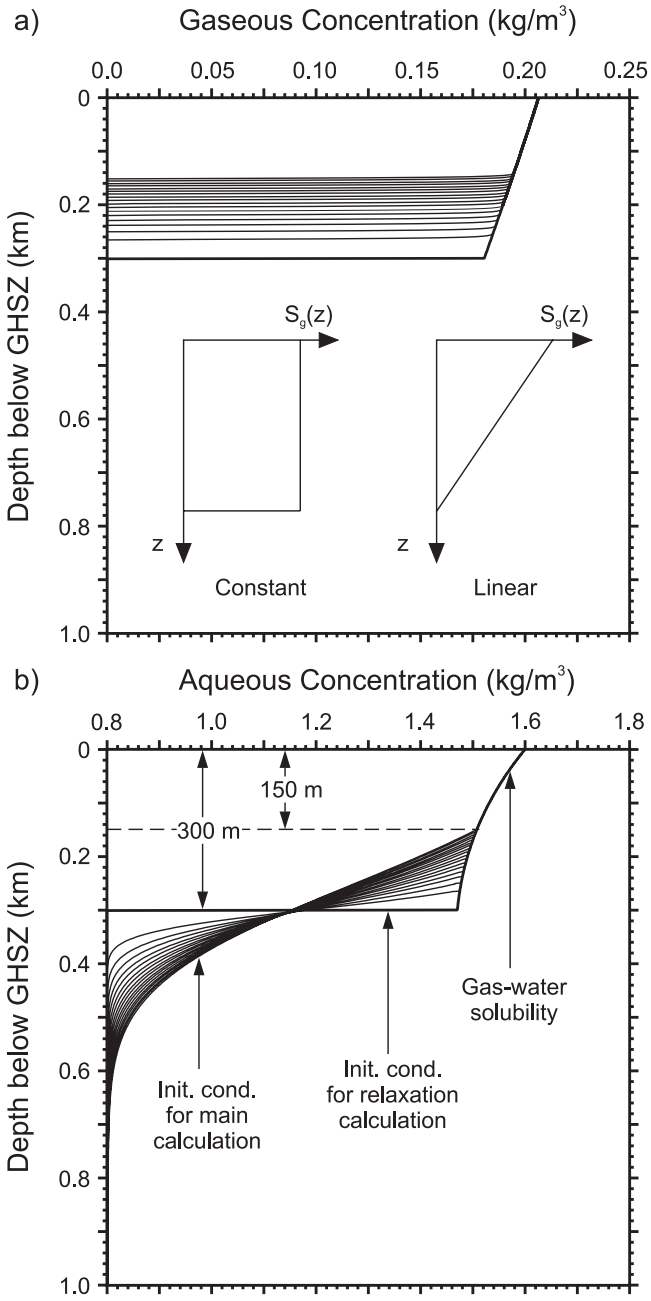

Figure 7. Gaseous (a) and aqueous (b) concentration profiles during the initial running-in calculation. Also shown are schematic representations of the constant and linearly decreasing gas-bubble volume profiles drawn in terms of gas volume fraction (S_g) and depth below seabed (z).

Analysis of field experiments by *Lallemand-Barres and Peaudecerf* [1978] suggests that the ratio of dispersivity to experimental scale is typically around 0.1 (summarized by *Fetter* [1999]). More extensive analysis of field results by *Gelhar* [1986] suggests that this ratio diminishes as the scale of the experiment increases, with values averaging about 0.06 for experiments conducted over 1 km; *Dagan* [1988] confirms that asymptotic behavior of the ratio is theoretically sound for stochastic porous media with a stationary logarithm of hydraulic conductivity. An approximate value for the dispersivity can be set by noting that dissolved methane is typically transported through lengths not exceeding 1000–2000 m from the base of the GHSZ (indicated in the results section) and so the dispersivity should be around 50 m.

[61] After the initial model runs, a sensitivity analysis was conducted for the model parameters, with particular attention paid to q_f, D and C_1. Since the mechanical dispersion term ($\alpha|u_f|$) is approximately one order of magnitude smaller than the diffusion term (χd_0), the analysis of D was carried out by varying only d_0 (although this parameter was allowed to exceed the likely limits imposed by the temperature range in order to account for uncertainties in χ and α).

5. Results

[62] The process of preconditioning the starting model by running the parameterization from an initial FGZ thickness of 300 m to the desired starting thickness of 150 m is illustrated in Figure 7. As the simulation matures, the aqueous concentration in the subsaturated zone approaches a quasi-steady state (quasi because of the evolving boundary conditions). This quasi-steady state is the correct starting point for the subsaturated part of the model, and each simulation is preceded with a running-in phase designed to produce this state.

5.1. Controls on FGZ Depletion and Growth

[63] The behavior of the FGZ is illustrated in Figure 8 as the main model parameters ($\dot{S}$, q_f, C_1, d_0 and S_{gc}) are individually varied. Although this approach does not consider the effect of parameter correlations, it does illustrate the relative importance of parameters in controlling the evolution of the FGZ. In this sensitivity analysis, each model simulation was run until the FGZ entirely depleted, until the FGZ reached a steady thickness, or until it exceeded 3 Ma runtime, at which point it was deemed to be unbounded.

[64] In simulations using the reference parameters (Table 1), the initial 150-m-thick FGZ was found to be unstable, and depleted entirely in approximately 0.5 Ma (Figure 8a). Furthermore, the sensitivity analysis shows that this unstable state, where the observed FGZ undergoes depletion, is a fairly robust result if the reference parameters are even approximately correct; depletion of the initial FGZ occurs within 0.2–2.0 Ma when $S_{gc} < 1.0\%$ (Figure 8b).

[65] Hydrate recycling driven by low to moderate sedimentation rates has only a weak influence on the lifetime of the FGZ (Figure 8c). Initially, one would expect the sedimentation rate to be a very important parameter controlling the rate of gas-zone depletion, or thickening, since this is the sole mechanism driving hydrate recycling in this passive margin environment. With the parameters of Table 1, sedimentation rates greater than 700 m Ma^{-1} would overcome the FGZ depletion at west Svalbard and cause net FGZ thickening. In this case, FGZ growth driven by hydrate recycling is not limited until the FGZ has reached a thickness of several hundred meters, at which point the gas–water solubility starts to increase from its solubility

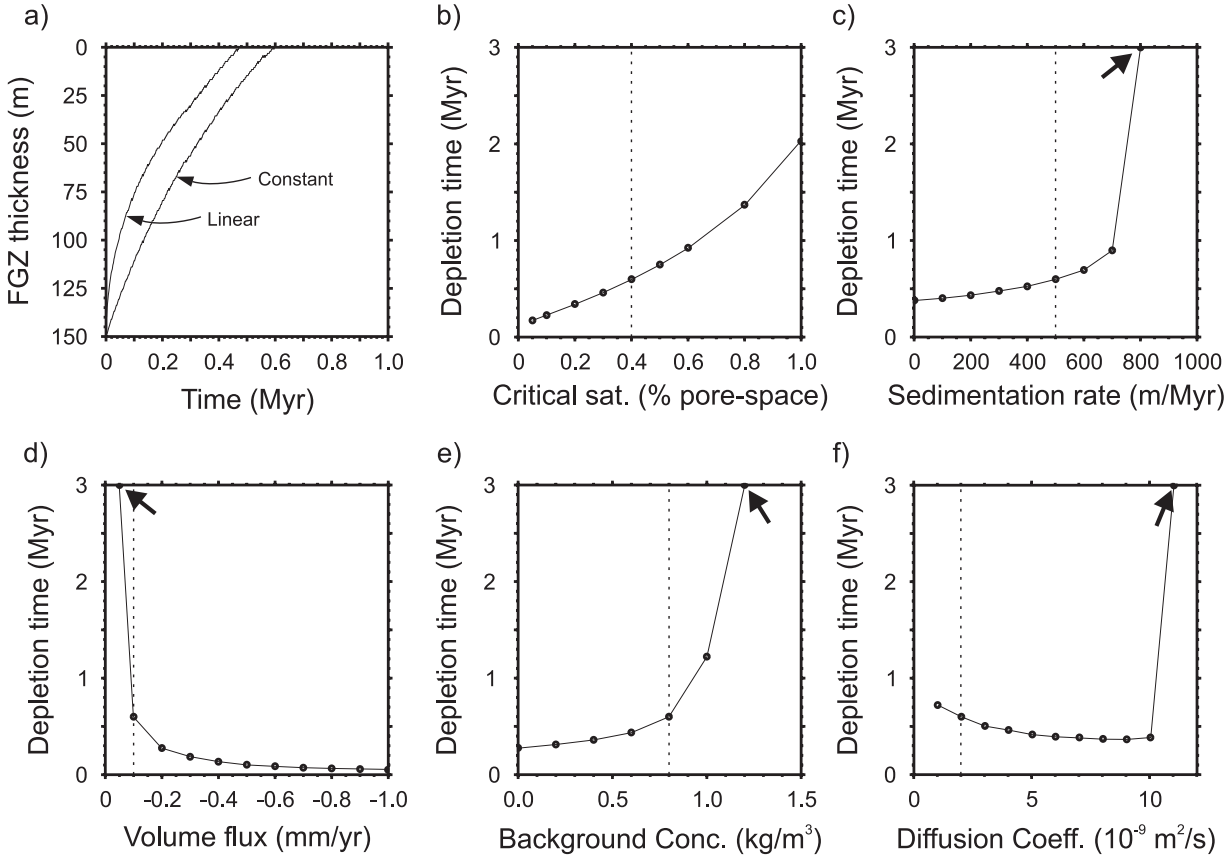

Figure 8. Results of model sensitivity analysis. (a) Thickness of the FGZ with increasing calculation time from the model parameterization of Table 1, but with initial gas concentration profiles altered to the constant and linearly decreasing shapes illustrated in Figure 7. (b–f) Time for total FGZ depletion from an initial thickness of 150 m and with the model parameters varied one parameter at a time. The points marked by black arrows did not achieve FGZ depletion when the model was stopped after 3 Ma. Vertical dashed lines represent the values in Table 1.

minimum (at approximately 600 mbsf at west Svalbard, Figure 4) and prevents further thickening.

[66] These results show that the evolution of the FGZ responds to sedimentation-driven hydrate recycling in one of two possible ways: (1) hydrate recycling has very little effect on the evolution of the FGZ, or (2) hydrate recycling drives FGZ thickening bounded only by the increasing gas–water solubility many hundreds of meters below the seafloor. The observed FGZ is in the range 150–200 m thick at west Svalbard, and is not even close to the depth of the solubility minimum at 600 mbsf. Indeed, most reports in the literature show that sub-BSR FGZs are in the range 10–250 m thick. The results described here indicate that if the reference parameters are approximately correct, then either the FGZ is currently in a state of transience, or an unstable equilibrium is somehow being maintained with $700 < \dot{S}$ [m Ma^{-1}] < 800. In the latter case, the FGZ would have a very low tolerance to changes in parameters such as the sedimentation rate.

[67] Aside from sedimentation rate, the three model parameters that can cause FGZ thickening are a low upward fluid flux (Figure 8d), a high background concentration of dissolved methane (Figure 8e), or a large diffusion coefficient (Figure 8f). Many gas hydrate systems with vigorous hydrate recycling (i.e., those in tectonically converging environments where the seabed is being uplifted, accretionary wedges for example) have relatively thin FGZs of a few tens of meters or less in thickness [e.g., *Minshull et al.*, 1994; *Hyndman et al.*, 2001; *Pecher et al.*, 2001] but also high rates of fluid advection, while sites with slow hydrate recycling (i.e., those in tectonically passive environments without seabed uplift) and low rates of fluid advection commonly have FGZs several tens to hundreds of meters thick [e.g., *Holbrook*, 2001; *Hornbach et al.*, 2004; *Bunz et al.*, 2005; *Carcione et al.*, 2005; *Westbrook et al.*, 2008]. It is clear from the results of this investigation, and from the above observations, that the production of gas by hydrate recycling can not be the dominant mechanism controlling the presence and properties of the FGZ and that its effects are offset by fluid advection and dispersion.

[68] In the remainder of this section we examine the advection–dispersion mechanisms driving FGZ growth by inspecting aqueous and gaseous concentration profiles as they develop from a model with no initial FGZ.

5.2. Free Gas Formation When Hydrate Recycling is Slow: The Solubility-Curvature Effect

[69] We set the rate of hydrate recycling to a vanishingly low value, then observe the formation of the FGZ under a range of fluid-flow conditions to determine when the FGZ

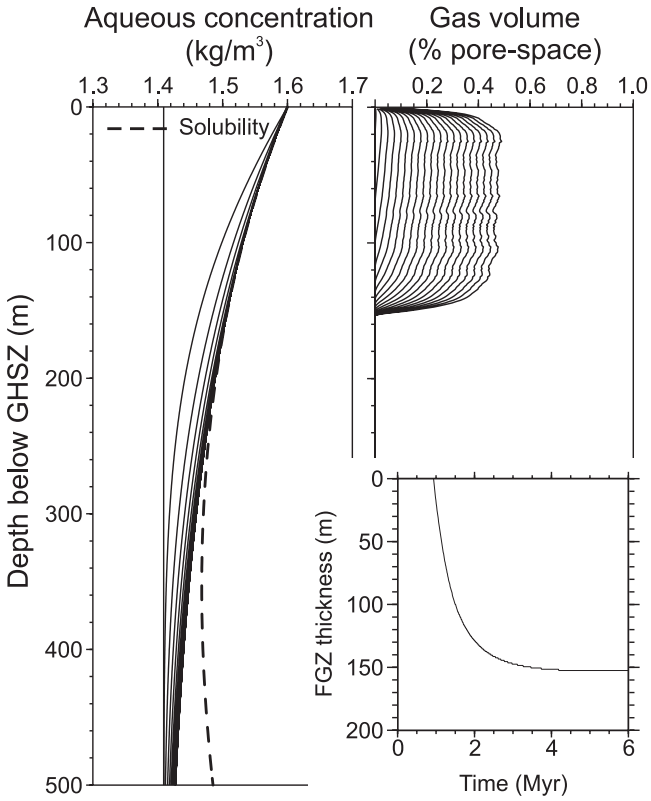

Figure 9. Dissolved and free gas concentration profiles, plotted at 0.25 Ma intervals, from a simulation with no initial FGZ and with hydrate recycling set to a vanishingly low rate. The simulation was conducted with C_1 = 1.409 kg m^{-3}, and with the remaining parameters those of Table 1. Inset shows the thickness of the FGZ with calculation time in the model. The gas–water solubility curve is plotted as the dashed line.

forms and becomes stable. Although this is physically implausible over long time periods, since hydrate recycling mechanisms are required to bring hydrate to the base of the GHSZ, this numerical trick helps clarify the role of other processes involved in FGZ formation.

[70] Starting from an initial aqueous concentration profile set to the background everywhere, we find the aqueous concentration gradually builds up toward the gas–water solubility curve and saturates pore water across a fixed depth range below the GHSZ when fluid flux (q_f) is low and background concentration (C_1) and the dispersion coefficient (D) are high (Figure 9). This is possible because the gas–water solubility curve is downward decreasing below the GHSZ; if the upward flow of under-saturated pore water is low, then downward diffusion of methane from the GHSZ becomes important and causes the aqueous concentration profile to flatten and try to exceed the downward decreasing solubility, consequently driving methane into the free-gas phase. The FGZ produced by this solubility-curvature effect rapidly obtains its preferred thickness (see the inset to Figure 9), which is controlled almost entirely by the values of q_f, C_1 and D. After the steady state thickness is achieved, the free-gas phase increases its concentration without further FGZ thickening.

5.3. Estimates of Fluid Flow

[71] The values of upward fluid flux, diffusion, and background dissolved-gas concentration required to maintain the thickness of the observed FGZ at west Svalbard by the solubility curvature effect were explored using an analytical approximation to equation (1). Using this approximation in conjunction with the gas–water solubility curve, we were able to define the model space for which the predicted steady state zone of saturated pore water (i.e., the FGZ) exists across a 150-m-thick layer beneath the GHSZ.

[72] The steady state is approximated by assuming $R_Q = 0$ in equation (2) (which has the consequence that $S_g = 0$ also), then setting the time derivative of equation (1) to zero and solving the resulting differential equation to find

$$C = B\left(\frac{\phi D}{\phi D - \alpha|q_f|}\right)^{\frac{\lambda q_f}{\alpha|q_f|}} + A, \tag{12}$$

where A and B are integration constants. The solution is completed using the boundary conditions $C = C_0$ when $z = z_0$ and $C = C_1$ when $z = z_1$ (i.e., C_1 is the background methane concentration, the bottom boundary condition, and C_0 is the solubility at the triple point, the top boundary condition) to find

$$A = C_0 - \frac{(C_0 - C_1)}{(n_0 - n_1)} n_0 \tag{13}$$

and

$$B = \frac{(C_0 - C_1)}{(n_0 - n_1)}, \tag{14}$$

where

$$n_m = \left(\frac{\phi_m D_m}{\phi_m D_m - \alpha|q_f|}\right)^{\frac{\lambda q_f}{\alpha|q_f|}} [m = 0, 1]. \tag{15}$$

The solution is insensitive to z_1 if its value is sufficiently large, in which case equation (12) gives a decaying exponential with increasing depth.

[73] The analytical solution is an approximation because of the requirement that $R_Q = 0$, which enables the liquid to become super-saturated without nucleating the free-gas phase. The quality of this approximation was assessed by fixing q_f, C_1 and D to the values used to produce the numerical result in Figure 9 then iteratively changing each parameter until the thickness of the zone of saturated liquid predicted from the difference between equation (12) and the gas–water solubility curve matched that of the numerical result. We found that the analytical solution underestimates the value of C_1 by approximately 1%, underestimates d_0 by approximately 12%, and overestimates $|q_f|$ by approximately 13%.

[74] If the observed FGZ thickness at the west Svalbard site is its steady state thickness, the region of model space that satisfies this criterion according to the difference between equation (12) and the solubility curve is illustrated in Figure 10. The maximum allowed value for C_1 was

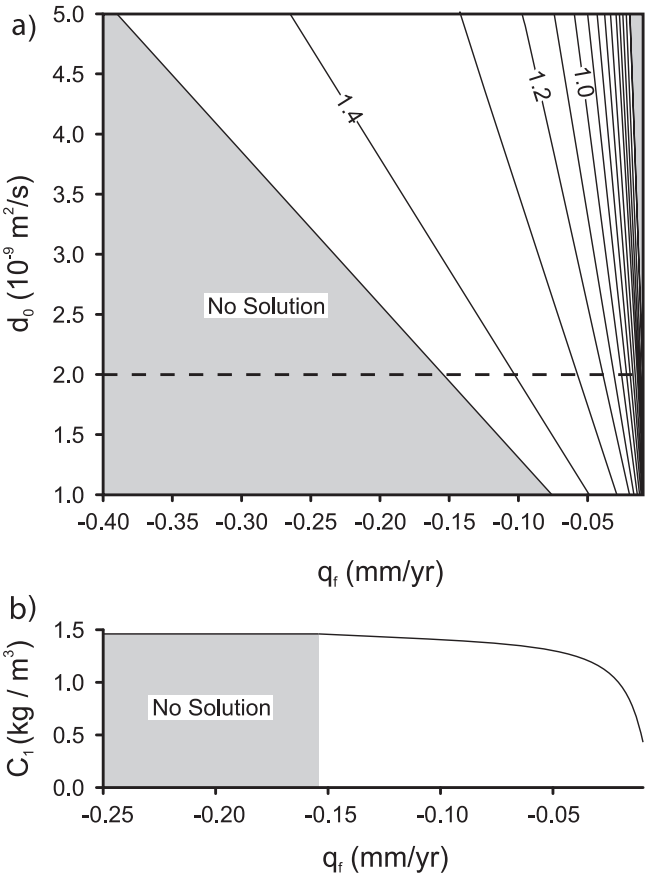

Figure 10. (a) Values of q_f, d_0 and C_1 that give a steady state FGZ of 150 m thickness according to the difference between equation (12) and the gas–water solubility curve. Contours show the value of C_1 (kg m^{-3}) with an upper limit defined by the solubility minimum at approximately 600 mbsf for the west Svalbard site. (b) Value of C_1 from part a plotted against q_f when $d_0 = 2 \times 10^{-9}$ m^2 s^{-1} (i.e., the profile along the dashed line in Figure 10a).

defined by the gas–water solubility minimum (at ≈ 600 mbsf in Figure 4).

[75] Given the best estimate for d_0 (2×10^{-9} m^2 s^{-1}), which is well constrained compared with q_f and C_1, these results indicate that the upward fluid flux generating a 150-m-thick FGZ by the solubility-curvature mechanism is $|q_f| < 0.15$ mm a^{-1}. In addition, we find that the range of values predicted for C_1 fall mostly on a plateau (Figure 10b), decreasing by only 15% from the maximum allowed value when $|q_f|$ decreases by 75%. The value of C_1 falls rapidly for $|q_f| < 0.05$ mm a^{-1}, but it should be remembered that the background concentration must satisfy the approximate condition that $C_1 > C_0/2$ ($C_1 > 0.8$ kg m^{-3} in this case) in order to create the hydrate at the base of the GHSZ from which the free gas is derived [*Davie and Buffett*, 2003b]. This means that, for a large range of cases where the BSR is underlain by a thick free-gas zone, the background concentration of dissolved gas is probably near to (but still less than) saturation at the gas–water solubility minimum several hundred meters below the GHSZ. The FGZ depletion we previously described for simulations using the reference parameters of Table 1 was a consequence of having a value of C_1 that was too low to allow FGZ formation by the solubility-curvature mechanism in all but the most extreme cases of low q_f and high D.

6. Discussion

[76] In the absence of mobile free-gas migration from deeper sources, the formation of both gas hydrate and underlying free gas is favored by greater upward flux of dissolved gases. *Xu and Ruppel* [1999] present an analytical expression for the rate of fluid flow (the critical flux) that is necessary for gas hydrate to be present at the base of the GHSZ. This is cast in terms of methane losses toward the seabed by diffusion along the solubility curve and the upward methane flux in advecting pore water, but uses a constant gas–water solubility and does not account for the downward hydrate flux caused by continuous hydrate recycling mechanisms (e.g., sedimentation). When the gas–water solubility decreases downward, as illustrated in Figure 4, the presence of hydrate and free gas at the triple point (respectively occupying sediment just above and just below) requires the dissolved-gas concentration profile to adopt the cusp shape defined by the solubility curves at the base of the GHSZ. In this case, there is no upward advective flux of liquid that can sustain the phases present at the triple point (and maintain the cusp-shaped concentration curve) without hydrate recycling. Such a cusp can only be maintained by an upward flow of mobile free gas through the sediments around the triple point, or by replacing diffusive losses from this point by a continual transfer of methane from the hydrate phase into local pore water. In the latter case, the reducing hydrate concentration must be replenished by a downward flux of hydrate transported in the sediment matrix.

6.1. The Importance of Hydrate Recycling

[77] If the downward hydrate flux is below the threshold at which it exactly replaces hydrate dissolving at the triple point, then diffusion along the hydrate–water solubility curve would cause the deepest occurrence of gas hydrate to migrate toward the seabed. Subsequently, the free gas below the triple point would dissolve, leading to a separation of the base of the zone containing hydrate and the top of the FGZ. This separation would be transient if the background concentration of dissolved gas is less than the concentration of the gas–water solubility minimum, but would occur in steady state if the background concentration exceeds the solubility minimum. In the latter case, however, the FGZ would be at and below the gas–water solubility minimum many hundreds of meters below the GHSZ. *Xu and Ruppel* [1999] also predict a separation of the base of the hydrate and the top of the FGZ, but this is an unphysical prediction, since it is based on an upward flow of supersaturated liquid below the triple point, does not consider the downward flux of hydrate, and uses a constant gas–water solubility below the triple point.

[78] If the downward flux of gas hydrate exceeds the threshold rate and moves hydrate to the base of the GHSZ, then the FGZ begins to form from a combination of hydrate recycling and the solubility curvature effect. The latter draws dissolved methane into the FGZ by diffusion and consequently increases the threshold hydrate flux needed to

maintain the presence of hydrate at the base of the GHSZ. The downward diffusive flux, however, is smaller than the diffusive flux toward the seabed because the gradient of the solubility curve is much lower in the FGZ than in the GHSZ.

6.2. Effect of Changing Permeability

[79] A system that has constant background concentration of dissolved gas across a wide area but also has lateral variations in upward fluid flux (due to variations in permeability, perhaps) will display variations in the thickness of the FGZ. This is due to the role of fluid flux in controlling the steady state FGZ thickness arising from the solubility-curvature effect and its role in depleting free gas that is outside the region of FGZ stability. Low fluid flux encourages formation of thick FGZs by the solubility-curvature effect, while rapid fluid flux encourages thin FGZs and also rapidly depletes free gas if the FGZ is intrinsically unstable.

[80] *Nimblett and Ruppel* [2003] analyze the formation of gas hydrate in permeable, porous and fractured media with the aim of understanding how hydrate clogs the fluid flow pathways and reduces the permeability. In their model, the permeability of a uniformly porous (unfractured) medium reduces by approximately two orders of magnitude in the first 10 Ma of gas hydrate accumulation. Thus as the concentration of overlying gas hydrate increases, the hydraulic conductance locally decreases in the GHSZ and the upward fluid flux locally reduces, causing the FGZ to thicken by the solubility curvature effect.

[81] The influence of focused, channelized flow (along faults, for example, and the lateral flow feeding faults) can not be explored directly with our model. Sparsely spaced, large scale faults do not pose much of a problem as the fluid flowing along these faults largely bypasses the modeled domain - that of a widespread, diffuse flow. Closely spaced, small-scale conduits (such as fractures) can be addressed more successfully, however, since the increased permeability will appear as a bulk property of the medium at the scale of most seismic observations, and, therefore, can be modeled adequately with the approach adopted here. For example, observations of S-wave splitting indicative of an azimuthal elastic anisotropy have been made at the west Svalbard study site, and are consistent with the existence of widespread, small-scale fractures that are vertically aligned in the direction of maximum principle stress [*Haacke and Westbrook*, 2006]. These fractures are likely to increase the vertical permeability of sediments which otherwise appear relatively homogeneous.

6.3. Wider Significance: General Application to BSRs in Continental Margins

[82] The solubility-curvature effect has been further assessed in a qualitative manner by *Haacke et al.* [2007], who discuss the likely influence of tectonic environment on the upward fluid flux, and thus as a first-order control on the presence and thickness of the sub-BSR FGZ. Analysis of eighteen study areas associated with natural gas hydrate in the literature showed that curvature of the gas–water solubility beneath the GHSZ is common, and is mainly controlled by water depth and local geothermal gradient. Areas in deep water with high geothermal gradients have strongly curved solubility profiles beneath the GHSZ, and are likely candidates for free-gas formation by the solubility-curvature effect. This is tempered by the rate of upward fluid flow, however, and it is reasonable to expect that FGZs in passive, rifted margins (where the upward fluid flux is low) are likely to be relatively thick, while FGZs in convergent-margin accretionary wedges (where the upward fluid flux is high) are likely to be relatively thin. In addition, *Haacke et al.* [2007] show that the presence of gas hydrate without an underlying FGZ (and thus without a BSR) in the northern Gulf of Mexico and Mackenzie Delta (Canadian Arctic) can be explained by a gas–water solubility that is downward increasing below the GHSZ coupled with relatively slow rates of hydrate recycling (i.e., these systems have no tectonic uplift of the seabed to drive rapid hydrate recycling rates). In these two areas, the FGZ is thus intrinsically unstable and the rate of hydrate recycling is not high enough to overcome the natural relaxation of these systems to their preferred gas-free state.

7. Summary and Conclusions

[83] By modeling the transport of dissolved methane through sediments overlain by gas hydrate, we have quantitatively evaluated the factors controlling the distribution and concentration of immobile free gas beneath the GHSZ. From this, we have provided new understanding of the formation and properties of the free-gas zone (FGZ) that is responsible for the BSR.

[84] The relationship between the gas–water solubility curve and the steady state aqueous concentration profile, produced by the competing effects of downward diffusion and upward advection, determines whether a free-gas zone is stable below the GHSZ. If the local solubility is downward decreasing below the GHSZ then free gas can persist in systems that have low upward flux of liquid, or high (but still subsaturated) concentrations of dissolved gas in deep pore fluid. If the gas–water solubility is downward increasing, or if the upward flux of pore water is high and concentration of gas dissolved in it is low, then the free-gas zone is intrinsically unstable. In this case, free gas produced by hydrate recycling is depleted by the upward flow of pore water as the system tries to relax to a gas-free state; a high rate of hydrate recycling is required if the FGZ is to exist in such systems. Neither hydrate recycling nor the solubility-curvature effect is dominant when the concentration of dissolved gas in deep liquids is high enough that it is able to saturate pore water well below the GHSZ and travel over part of its upward migration path in the free-gas phase.

7.1. General Conclusions

[85] (1) Gas is produced beneath the GHSZ by a combination of hydrate recycling and the solubility-curvature effect. Both mechanisms require the presence of gas hydrate at the base of the GHSZ and a downward flux of hydrate (relative to the hydrate–liquid–gas triple point) that can maintain this hydrate distribution;

[86] (2) The upward flux of liquid and the background concentration of dissolved gas at depth determine the relative importance of the solubility-curvature effect in producing a FGZ;

[87] (3) Free gas generated by the solubility-curvature effect typically forms low concentrations of gas across a

thick zone (up to a few hundred meters thick) with steady state thickness;

[88] (4) Sediment-hosted gas hydrate has the potential to exist without an underlying FGZ if the hydrate recycling rate is low, and if the upward flux of liquid is high and contains low concentrations of dissolved gas. In these scenarios, free gas produced by hydrate recycling is rapidly depleted by the upward flux of subsaturated pore water.

7.2. Site-Specific Conclusions

[89] (1) At the study area west of Svalbard, sedimentation-driven hydrate recycling is not rapid enough to produce the observed sub-BSR FGZ. The thickness of this FGZ (approximately 150 m) is primarily attributable to the solubility-curvature effect;

[90] (2) Pressure and temperature changes associated with the last deglaciation did not contribute to the sub-BSR FGZ at west Svalbard;

[91] (3) The 150-m-thick FGZ observed at west Svalbard would require 10^5–10^6 years to deplete in response to changes in fluid flow or the conditions controlling hydrate recycling;

[92] (4) If the observed FGZ at west Svalbard is stable, then the upward fluid flux through this system is unlikely to exceed 0.15 mm a^{-1} and the concentration of dissolved gas in deep fluid is probably close to, but still less than, the gas–water solubility minimum at approximately 600 mbsf.

Appendix A: Hydrate Dissociation Due to Sedimentation

[93] Lengthening of the sediment column is calculated by conserving solid volume with a steady-state compaction curve, equation (5), and with a sedimentation rate of magnitude $\dot{S}$. The rate of solid sediment volume added to the system per unit area is $\dot{S}[1-\phi_0]$. For a basement depth z_b and a seabed depth change Δz_s caused by a unit time interval of sedimentation, conservation of solid volume gives

$$\dot{S}[1-\phi_0] = \int_0^{z_b+\Delta z_s} [1-\phi(z)]dz - \int_0^{z_b} [1-\phi(z)]dz. \quad \text{(A1)}$$

[94] Let maximum compaction occur at depth z_m, after which the porosity is constant (ϕ_m). If $z_m < z_b$, then equation (A1) simplifies to

$$\Delta z_s = -\dot{S}[1-\phi_0]/[1-\phi_m]. \quad \text{(A2)}$$

[95] The applicability of equation (A2) to the sediments of the west Svalbard site can be evaluated using $\phi_m = 0.06$, a median value for shales [*Allen and Allen*, 2005], to find $z_m = -\lambda\, ln[\frac{\phi_m}{\phi_0}] = 2300$ m. The sediment thickness above oceanic crust at this site is approximately 5000 m [*Ritzmann et al.*, 2004], much greater than the estimated maximum compaction depth: equation (A2) is therefore appropriate.

[96] Additional sediment causes the oceanic plate on which it sits to displace mantle material by isostasy. Equating the mass of additional sediment deposited at the seabed to the mass of displaced mantle material, we find

$$\dot{S}[1-\phi_0]\rho_s = V_m\rho_m, \quad \text{(A3)}$$

where ρ_s is the sediment grain density, V_m is the volumetric rate of mantle displacement and ρ_m is the density of displaced mantle material ($\rho_m = 3300$ kg m^{-3}). The vertical isostatic movement of the plate per unit area and per unit time is given by V_m. The net rate of seabed movement is given by $\Delta z_s + V_m$.

Appendix B: Hydrate Dissociation Due to Deglaciation

[97] This section deals with the effect of a global deglaciation on the gas hydrate site west of Svalbard and seeks to quantify the time-dependent hydrate recycling caused by this deglaciation.

[98] Global deglaciation at the end of the Pleistocene is thought to have occurred over the period 18–5 ka before present (BP), with the current Holocene environment mostly complete by 7 ka BP [*Lowe and Walker*, 1997]. However, the transition from glacial to interglacial conditions was not accompanied by simple, linear changes in sea level and oceanic or climatic temperatures. Benthic foraminifera analyzed offshore the mid-Norwegian margin (in approximately 1000 m water depth) have shown that the warm currents which move up this margin, past western Svalbard, and into the Arctic began abruptly near the end of the Younger Dryas [*Kristensen et al.*, 2003; *Mienert et al.*, 2005]. That the bottom water along this margin warmed discontinuously at this time (approximately 10–12 ka BP) and has remained warm until the present-day is consistent with global temperature patterns [e.g., *Alley et al.*, 1993] and with local sea-surface palaeo-temperature measurements made in the west Spitsbergen area [*Hald et al.*, 2004].

[99] The thermal effect of Pleistocene–Holocene deglaciation was probably manifested in the gas-hydrate bearing sediments west of Svalbard by a step-change of bottom water temperature. The magnitude of this bottom water temperature change has not been measured, but is estimated at +0.4 °C given the current bottom water temperature and estimated deep-water temperatures of −1.3 °C in the Northern Atlantic and Pacific during glacial times [*Waelbroeck et al.*, 2002; *Ohkushi et al.*, 2003].

[100] To quantify sea level change since the last glacial maximum (approximately 18–19 ka BP), the curve of *Fairbanks* [1989] is used, which gives a net sea level rise of 121 ± 5 m. This value is generally accepted as indicative of the global sea level change and is consistent with measurements made in disparate areas around the world by a variety of methods [e.g., *Peltier*, 2002].

[101] Steady state geotherms for the present-day (PD) and late glacial maximum (LGM) are plotted for the Svalbard site with relaxing geotherms calculated for a series of time-intervals since a discontinuous bottom water temperature change of +0.4°C, Figure 6. This diagram also shows the phase stability curves for pure methane hydrate in 3.5 wt. % NaCl solution and at pressures and temperatures appropriate for the PD and the LGM. The relaxing geotherm calculated 10 ka after the bottom water warming (which makes the temperature change approximately coeval with the end of the Y. Dryas) intersects the present-day methane hydrate stability curve at the seismically derived BSR depth with a heat flow of 100 mW m^{-2} when the conductivity is 1.156 W m^{-1} K^{-1}.

[102] The time-dependent position of the triple point since the LGM is calculated by simultaneously solving the time-dependent geotherm and hydrate phase stability equations for a pressure that depends on the global sea level and for temperature that depends on a bottom water warming event of +0.4 °C that occurred 10 ka BP. The results are illustrated in Figure 6, where the global sea level curve is described by fitting an analytical function to the sea level data of *Fairbanks* [1989]: $z_w = (z_w^{PD} - A) + Ae^{-h^2(t-t')^2}$ when $t > t'$ and $z_w = z_w^{PD}$ when $t < t'$. z_w^{PD} is the present-day water depth (1394 m), A is the net sea level change between the last glacial maximum and the present-day (121 m), h is the width of the Gaussian function ($h = 1.4 \times 10^{-4}$) and t' is a time parameter ($t' = 6000$ years).

[103] **Acknowledgments.** RRH wishes to thank Roy Hyndman (Geological Survey of Canada) for his ongoing support in all its forms, Ted Irving (Geological Survey of Canada) for reminding me of the importance of tenacity in science, and Maarten Vanneste (Norwegian Geotechnical Institute) for his geological insight. RRH was supported by the University of Birmingham and, later, by the University of Victoria and the Geological Survey of Canada.

References

Allen, P. A., and J. R. Allen (2005), *Basin Analysis: Principles and Applications*, 2nd ed., Blackwell Publishing, Malden, MA.

Alley, R. B., et al. (1993), Abrupt accumulation increase at the Younger Dryas termination in the GISP2 ice core, *Nature*, *362*, 527–529.

Amili, P., and Y. C. Yortsos (2006), Darcian dynamics: A new approach to the mobilization of a trapped phase in porous media, *Transp. Porous Media*, *64*, 25–49.

Athy, L. F. (1930), Density, porosity, and compaction of sedimentary rocks, *AAPG Bull.*, *14*, 1–24.

Attia, A. M. (2005), Effects of pertrophysical rock properties on tortuosity factor, *J. Petrol. Sci. Eng.*, *48*, 185–198.

Bangs, N. L. B., R. J. Musgrave, and A. M. Tréhu (2005), Upward shifts in the southern Hydrate Ridge gas hydrate stability zone following postglacial warming, offshore Oregon, *J. Geophys. Res.*, *110*, B03102, doi:10.1029/2004JB003293.

Bear, J. (1979), *Hydraulics of Groundwater*, McGraw-Hill, New York.

Beicher, R. J. (2000), *Physics for Scientists and Engineers*, Saunders College, Orlando.

Bondino, I., S. R. McDougall, and G. Hamon (2005), Pore network modeling of heavy-oil depressurization: A parametric study of factors affecting critical gas saturation and three-phase relative permeabilities, *SPE J.*, *10*(2), 196–205.

Buffett, B. A., and D. Archer (2004), Global inventory of methane clathrate: Sensitivity to changes in the deep ocean, *Earth Planet. Sci. Lett.*, *227*(3–4), 185–199.

Bunz, S., J. Mienert, M. Vanneste, and K. Andreassen (2005), Gas hydrates at the Storegga slide: Constraints from an analysis of multicomponent, wide-angle seismic data, *Geophysics*, *70*(5), B19–B34.

Butt, F. A., A. Elverhoi, A. Solheim, and C. F. Forsberg (2000), Deciphering Late Lenozoic development of the western Svalbard margin from ODP 986 results, *Mar. Geol.*, *169*, 373–390.

Carcione, J. M., D. Gei, G. Rossi, and G. Madrussani (2005), Estimation of gas-hydrate concentration and free-gas saturation at the Norwegian-Svalbard continental margin, *Geophys. Prospect.*, *53*, 803–810.

Corapcioglu, M. Y., A. Cihan, and M. Drazenovic (2004), Rise velocity of an air bubble in porous media: Theoretical studies, *Water Resour. Res.*, *40*, W04214, doi:10.1029/2003WR002618.

Dagan, G. (1988), Time-dependent macrodispersion for solute transport in anisotropic heterogeneous media, *Water Resour. Res.*, *24*(9), 1491–1500.

Davie, M. K., and B. A. Buffett (2001), A numerical model for the formation of gas hydrate below the seafloor, *J. Geophys. Res.*, *106*(B1), 497–514.

Davie, M. K., and B. A. Buffett (2003a), A steady state model for marine hydrate formation: Constraints on methane supply from pore water sulphate profiles, *J. Geophys. Res.*, *108*(B10), 2495, doi:10.1029/2002JB002300.

Davie, M. K., and B. A. Buffett (2003b), Sources of methane for marine gas hydrate: Inferences from a comparison of observation and numerical models, *Earth Planet. Sci. Lett.*, *206*, 51–63.

Du, C., and Y. C. Yortsos (1999), A numerical study of the critical gas saturation in a porous medium, *Transp. Porous Media*, *35*, 205–225.

Duan, Z., N. Moller, J. Greenberg, and J. H. Weare (1992a), The prediction of methane solubility in natural waters to high ionic strength: From 0 to 250°c and from 0 to 1600 bar, *Geochim. Cosmochim. Acta*, *56*, 1451–1460.

Duan, Z., N. Moller, and J. H. Weare (1992b), An equation of state for the CH4-CO2-H2O system: 1. Pure systems from 0 to 1000°c and 0-8000 bar, *Geochim. Cosmochim. Acta*, *56*, 2605–2617.

Egeberg, P. K., and G. R. Dickens (1999), Thermodynamic and pore water halogen constraints on gas hydrate distribution at ODP site 997 (Blake Ridge), *Chem. Geol.*, *153*, 53–79.

Eiken, O., and K. Hinz (1993), Contourites in the Fram Strait, *Sediment. Geol.*, *82*, 15–32.

Fairbanks, R. G. (1989), A 17000-year glacio-eustatic sea level record: Influence of glacial melting rates on the Younger Dryas event and deep-ocean circulation, *Nature*, *342*, 637–642.

Fetter, C. W. (1999), *Contaminant Hydrogeology*, 2nd ed., Prentice-Hall, New Jersey.

Firoozabadi, A., B. Ottesen, and M. Mikkelsen (1992), Measurements of supersaturation and critical gas saturation, *SPE Formation Evaluation*, *7*(4), 337–344.

Foucher, J. P., H. Nouzé, and P. Henry (2002), Observation and tentative interpretation of a double BSR on the Nankai slope, *Mar. Geol.*, *187*, 161–175.

Gelhar, L. (1986), Stochastic subsurface hydrology from theory to applications, *Water Resour. Res.*, *22*(9S), 135S–145S.

Grevemeyer, I., and H. Villinger (2001), Gas hydrate stability and the assessment of heat flow through continental margins, *Geophys. J. Int.*, *145*, 647–660.

Haacke, R. R., and G. K. Westbrook (2006), A fast, robust method for detecting and characterising azimuthal anisotropy with marine PS converted waves, and its application to the west Svalbard continental slope, *Geophys. J. Int.*, *167*, 1402–1412, doi:10.1111/j.1365-246X.2006.031.x.

Haacke, R. R., G. K. Westbrook, and R. D. Hyndman (2007), Gas hydrate, fluid flow and free-gas: Formation of the bottom-simulating reflector, *Earth Planet. Sci. Lett.*, *261*, 407–420, doi:10.1016/j.epsl.2007.07.008.

Hald, M., H. Ebbesen, M. Forwick, F. Godtliebsen, L. Khohomenko, S. Korsun, L. R. Olsen, and T. O. Vorren (2004), Holocene palaeoceanography and glacial history of the west Spitsbergen area, Euro-Arctic margin, *Quat. Sci. Rev.*, *23*, 2075–2088.

Helgerud, M. B., J. Dvorkin, A. Nur, A. Sakai, and T. S. Collett (1999), Elastic wave velocity in marine sediments with gas hydrates: Effective medium modelling, *Geophys. Res. Lett.*, *26*(13), 2021–2024.

Holbrook, W. S. (2001), Seismic studies of the Blake Ridge: Implications for hydrate distribution, methane exulsion and free gas studies, in *Natural Gas hydrates: Occurrence, Distribution and Detection, Geophysical Monographs*, vol. 124, edited by C. K. Paull and W. P. Dillon, pp. 235–256, American Geophysical Union, Washington, DC.

Hornbach, M. J., D. M. Saffer, and W. S. Holbrook (2004), Critically pressured free-gas reservoirs below gas-hydrate provinces, *Nature*, *427*(6970), 142–144.

Hutchison, I. (1985), The effects of sedimentation and compaction on oceanic heat flow, *Geophys. J. R. Astron. Soc.*, *82*, 439–459.

Huyakorn, P. S., and G. F. Pinder (1983), *Computational Methods in Subsurface Flow*, Academic Press, London.

Hyndman, R. D., and E. E. Davis (1992), A mechanism for the formation of methane hydrate and seafloor bottom-simulating-reflectors by vertical fluid expulsion, *J. Geophys. Res.*, *97*(B5), 7025–7041.

Hyndman, R. D., and G. D. Spence (1992), A seismic study of methane hydrate marine bottom-simulating-reflectors, *J. Geophys. Res.*, *97*(B5), 6683–6698.

Hyndman, R. D., G. F. Moore, and K. Moran (1993), Velocity, porosity and porefluid loss from the Nankai subduction zone accretionary prism, in *Proceedings of the ODP, Scientific Results*, vol. 131, edited by I. A. Hill, A. Taira, and J. V. Firth, pp. 211–220, College Station, TX.

Hyndman, R. D., G. D. Spence, T. Yuan, and E. E. Davis (1994), Regional geophysics and structural framework of the Vancouver Island margin accretionary prism, in *Proceedings of the ODP, Initial Reports*, vol. 146 I, edited by G. K. Westbrook, B. Carson, and R. J. e. Musgrave, pp. 399–419, College Station, TX.

Hyndman, R. D., G. D. Spence, R. Chapman, M. Riedel, and R. N. Edwards (2001), Geophysical studies of marine gas hydrate in northern Cascadia, in *Natural Gas Hydrates: Occurrence, Distribution and Detection, Geophysical Monographs*, vol. 124, edited by C. K. Paull and W. P. Dillon, pp. 273–296, American Geophysical Union, Washington, DC.

Jansen, E., and M. E. Raymo (1996), North-Atlantic-Arctic gateways II, *Initial Rep. of the ODP*, *162*, 5–20.

Jung, W., and P. Vogt (2004), Effects of bottom water warming and sea level rise on Holocene hydrate dissociation and mass wasting along the Norwegian–Barents continental margin, *J. Geophys. Res.*, *109*, B06104, doi:10.1029/2003JB002738.

Kortekaas, T. F. M., and F. V. Poelgeest (1991), Liberation of solution gas during pressure depletion in virgin and watered-out oil reservoirs, *SPE Resour. Eval. Eng.*, *6*(1), 329–325.

Kristensen, K. D., T. Dokken, H. Haflidason, E. Jansen, M. Meland, and W. Lekens (2003), Palaeoenvironmental studies – Upper Storegga margin area: Palaeotemperature reconstructions, late glacial to holocene scenario, *NHT-B44-510104900 100-07/02*, p. Department of Geology University of Bergen.

Krooss, B. M., and D. Leythaeuser (1988), Eperimental measurements of the diffusion parameters of light hydrocarbons in water-saturated sedimentary rocks: Ii results and geochemical significance, *Org. Geochem.*, *12*, 91–108.

Kvenvolden, K. A., L. A. Barnard, and D. H. Cameron (1983), Pressure core barrel: Applications to the study of gas hydrates, DSDP site 533 Leg 76, *Proc. DSDP, Initial Rep.*, *76*, 367–375.

Lallemand-Barres, A., and P. Peaudecerf (1978), Recherche des relations entre la valeur de la dispersivité macroscopique d'un aquifére, ses autres caractéristiques et les conditions de mesure, *Bulletin du Bureau de Recherches Geologiques et Minieres Sect*, *3*(4), 277–287.

Liu, X., and P. B. Flemings (2007), Dynamic multiphase flow model of hydrate formation in marine sediments, *J. Geophys. Res.*, *112*, B03101, doi:10.1029/2005JB004227.

Lowe, J. J., and M. J. C. Walker (1997), *Reconstructing Quaternary Environments*, 2nd ed., Addison Wesley, London.

Lu, W. J., I. M. Chou, R. C. Burruss, and M. Z. Yang (2006), In Situ study of mass transfer in aqueous solutions under high pressures via Raman Spectroscopy: A new method for the determination of diffusion coefficients of methane in water near hydrate formation conditions, *Appl. Spectrosc.*, *60*(2), 122–129.

MacKay, M. E., R. D. Jarrard, G. K. Westbrook, and R. D. Hyndman (1994), Origin of bottom-simulating reflectors: Geophysical evidence from the Cascadia accretionary prism, *Geology*, *22*, 459–462.

Marulanda, C., P. J. Culligan, and J. T. Germaine (2000), Centrifuge modeling of air spargins – A study of air flow through saturated porous media, *J. Hazard. Mater.*, *72*, 179–215.

McDougall, S. R., and K. S. Sorbie (1999), Estimation of critical gas saturation during pressure depletion in virgin and waterflooded reservoirs, *Petrol. Geosci.*, *5*, 229–233.

Meakin, P., G. Wagner, A. Vedik, H. Amundsen, J. Feder, and T. Jøssang (2000), Invasion percolation and secondary migration: Experiments and simulations, *Mar. Petrol. Geol.*, *17*, 777–795.

Mienert, J., M. Vanneste, S. Bunz, K. Andreassen, H. Haflidason, and H. P. Sejrup (2005), Ocean warming and gas hydrate stability on the mid-Norwegian margin at the Storegga slide, *Mar. Petrol. Geol.*, *22*, 233–244.

Milton, D. J. (1976), Methane hydrate in the sea-floor – A significant resource?, in *The Future Supply of Nature-Made Petrolem and Gas Technical Reports*, edited by R. F. Meyer, pp. 927–943, Pergamon, NY.

Minshull, T., and R. White (1989), Sediment compaction and fluid migration in the Makran accretionary prism, *J. Geophys. Res.*, *94*(B6), 7387–7402.

Minshull, T. A., S. C. Singh, and G. K. Westbrook (1994), Seismic velocity structure at a gas hydrate reflector, offshore western Columbia, from full waveform inversion, *J. Geophys. Res.*, *99*(B3), 4715–4734.

Moulu, J. C. (1989), Solution-gas drive: Experiments and simulation, *J. Petrol. Sci. Eng.*, *2*, 379–386.

Nimblett, J., and C. Ruppel (2003), Permeability evolution during the formation of gas hydrates in marine sediments, *J. Geophys. Res.*, *108*(B9), 2420, doi:10.1029/2001JB001650.

Ohkushi, K., A. Suzuki, H. Kawahata, and L. P. Gupta (2003), Glacial-interglacial deep-water changes in the NW Pacific inferred from single foraminiferal $\delta^{18}O$ and $\delta^{13}C$, *Mar. Micropalaeontol.*, *48*, 281–290.

Oldenburg, C. M., and J. L. Lewicki (2006), On leakage and seepage of co2 from geologic storage sites into surface water, *Environ. Geol.*, *50*, 691–705, doi:10.1007/s00254-006-0242-0.

Paull, C. K., W. Ussler, and W. S. Borowski (1994), Sources of biogenic methane to form marine gas hydrates: In-situ production or upward migration, in *International Conference on Natural Gas Hydrates*, vol. 715, edited by E. D. Sloan, pp. 392–409, Annals of the New York Academy of Sciences, New York.

Pecher, I. A., N. Kukowski, C. R. Ranero, and R. VonHuene (2001), Gas hydrates along the Peru and middle America trench systems, in *Natural Gas Hydrates: Occurrence, Distribution and Detection, Geophysical Monographs*, vol. 124, edited by C. Paull and W. P. Dillon, pp. 257–271, American Geophysical Union, Washington, DC.

Peltier, W. R. (2002), On eustatic sea level history: Last glacial maximum to Holocene, *Quat. Sci. Rev.*, *21*, 377–396.

Rehder, G., P. W. Brewer, E. T. Peltzer, and G. Friedrich (2002), Enhanced lifetime of methane bubble streams within the deep ocean, *Geophys. Res. Lett.*, *29*(15), 1731, doi:10.1029/2001GL013966.

Rempel, A. W., and B. A. Buffett (1997), Formation and accumulation of gas hydrate in porous media, *J. Geophys. Res.*, *102*(B5), 10151–10,164.

Ritzmann, O., W. Jokat, W. Czuba, A. Guterch, R. Mjelde, and Y. Nishimura (2004), A deep seismic transect from Hovgard Ridge to northwestern Svalbard across the continental-ocean transition: A sheared margin study, *Geophys. J. Int.*, *157*, 683–702.

Roosevelt, A. E., and M. Y. Corapcioglu (1998), Air bubble migration in a granular porous medium: Experimental studies, *Water Resour. Res.*, *34*(5), 1131–1142.

Sachs, W. (1998), The diffusional transport of methane in liquid water: Method and result of experimental investigation at elevated pressure, *J. Petrol. Sci. Eng.*, *21*, 153–164.

Schowalter, T. T. (1979), Mechanics of secondary hydrocarbon migration and entrapment, *Bull. Am. Assoc. Petrol. Geol.*, *63*, 723–760.

Shipley, T. H., M. H. Houston, R. T. Buffler, F. J. Shaub, K. J. McMillen, J. W. Ladd, and J. L. Worzel (1979), Seismic reflection evidence for the widespread occurrence of possible gas hydrate horizons on continental slopes and rises, *Am. Assoc. Petrol. Geol. Bull.*, *63*, 2204–2213.

Singh, S. C., T. A. Minshull, and G. D. Spence (1993), Velocity structure of a gas hydrate reflector, *Science*, *260*, 204–207.

Sloan, E. D. (1990), *Clathrate Hydrates of Natural Gases*, 1st ed., Marcel Dekker Inc, NY.

Stöhr, M., and A. Khalili (2006), Dynamic regimes of buoyancy-affected two-phase flow in unconsolidated prous media, *Phys. Rev. E*, *73*, 036301, doi:10.1103/PhysRevE.73.036301.

Tsimpanogiannis, I. N., and Y. C. Yortsos (2002), Model for the gas evolution in a porous medium driven by solute diffusion, *Environ. Energy Eng.*, *48*(11), 2690–2710.

Tsimpanogiannis, I. N., and Y. C. Yortsos (2004), The critical gas saturation in a porous medium in the presence of gravity, *J. Colloid Interface Sci.*, *270*, 388–395.

Vanneste, M., S. Guidard, and J. Mienert (2005a), Arctic gas hydrate provinces along the western Svalbard continental margin, in *Onshore-Offshore Relationships on the North Atlantic Margin*, edited by B. T. G. Wandas et al., pp. 271–284, Norwegian Petroleum Society Special Publication, Elsevier Sciences, Amsterdam.

Vanneste, M., S. Guidard, and J. Mienert (2005b), Bottom-simulating reflections and geothermal gradients across the western Svalbard margin, *Terra Nova*, *17*(6), 515–516, doi:10.1111/j.1365-3121.2005.00643.x.

Vorren, T. O., J. S. Laberg, F. Blaume, J. A. Dowdeswell, N. H. Kenyon, J. Mienert, J. Rumohr, and F. Werner (1998), The Norwegian-Greenland sea continental margins: Morphology and late quaternary sedimentary processes and environment, *Quat. Sci. Rev.*, *17*, 273–302.

Waelbroeck, C., L. Labeyrie, E. Michel, J. C. Duplessy, J. F. McManus, K. Lambeck, E. Balbon, and M. Labracherie (2002), Sea-level and deep water temperature changes derived from benthic foraminifera isotopic records, *Quat. Sci. Rev.*, *21*, 295–305.

Wang, K., R. D. Hyndman, and E. E. Davis (1993), Thermal effects of sediment thickening and fluid expulsion in accretionary prisms: Model and parameter analysis, *J. Geophys. Res.*, *98*(B6), 9975–9984.

Westbrook, G. K., et al. (2005), Measurement of P- and S-wave velocities, and the estimation of hydrate concentration at sites in the continental margin of Svalbard and the Storegga region of Norway, *Proc. 5th Int. Conf. Gas Hydrates*, *3*, 726–735.

Westbrook, G. K., et al. (2008), Estimation of gas-hydrate concentration from multi-component seismic data at sites on the continental margins of NW Svalbard and the Storegga region of Norway, *Mar. Pet. Geol.*, doi:10.1016/j.marpetgeo.2008.02.003.

White, R. S. (1977), Gas hydrate layers trapping free-gas in the gulf of oman, *Earth Planet. Sci. Lett.*, *42*, 114–120.

Xu, W., and L. N. Germanovich (2006), Excess pore pressure resulting from methane hydrate dissociation in marine sediments: A theoretical approach, *J. Geophys. Res.*, *111*, B01104, doi:10.1029/2004JB003600.

Xu, W., and C. Ruppel (1999), Predicting the occurrence, distribution and evolution of methane gas hydrate in porous marine sediments, *J. Geophys. Res.*, *104*(B3), 5081–5095.

Zatsepina, O. Y., and B. A. Buffett (1998), Thermodynamic conditions for the study of gas hydrates in the seafloor, *J. Geophys. Res.*, *103*(B10), 24,127–24,139.

Zatsepina, O. Y., and B. A. Buffet (2001), Experimental study of the stability of CO_2 hydrate in a porous medium, *Fluid Phase Equilibria*, *192*, 85–102.

R. R. Haacke, Geological Survey of Canada, Pacific Geoscience Centre, 9860 West Saanich Road, BC V8L 4B2, Canada. (rhaacke@nrcan.gc.ca)

M. S. Riley and G. K. Westbrook, School of Geography, Earth and Environmental Sciences, University of Birmingham, Edgbaston, B15 2TT, UK.